High Velocity Cloud Interactions With Their Ambient Environment

by

Jeffrey Gritton

(Under the Direction of Robin Shelton)

Abstract

High velocity clouds (HVCs) are collections of gas around the Milky Way galaxy and other galaxies with masses ranging from tens of thousands of solar masses to millions of solar masses. These cool clouds can potentially supply new cool material to the disks of galaxies. Many unanswered questions exist about HVCs; e.g. "How do HVCs form?", "How long can HVCs survive while interacting with the hot ambient material?", and "How do HVCs affect, and how are they affected by, our Galaxy?"

Using detailed multi-dimensional numerical simulations, this study focuses on how HVCs interact with their ambient environments and how these interactions affect the cloud's metal concentration, condensation and evaporation rates, and morphology. Using the results of these simulations this study suggests methods to determine the origins of HVCs based on observed metal concentrations, and how initial parameter space affects the condensation of ambient material onto HVCs.

Index words: High Velocity Clouds, Interstellar Medium, Intergalactic Medium, Galactic Evolution, Hydrodynamics, Magnetohydrodynamics, Numerical Simulation

High Velocity Cloud Interactions With Their Ambient Environment

by

Jeffrey Gritton

B.S., Kent State University Kent, 2006

M.S., Ball State University Muncie, 2008

A Dissertation Submitted to the Graduate Faculty

of The University of Georgia in Partial Fulfillment

of the

Requirements for the Degree

Doctor of Philosophy

Athens, Georgia

2017

High Velocity Cloud Interactions With Their Ambient Environment

by

Jeffrey Gritton

Approved:

Major Professor: Robin Shelton

Committee: Loris Magnani
Phillip Stancil

Electronic Version Approved:

Suzanne Barbour
Dean of the Graduate School
The University of Georgia
May 2017

Dedication

This dissertation is dedicated to my friends, family, and mentors. Without your constant support and assistance none of this would have been possible. Thank you all.

Acknowledgments

I would like to thank all those that have assisted me in my work. I would like to thank Dr. Robin Shelton for her guidance and tutelage in my time at The University of Georgia. I would like to thank the the faculty of the Physics Department at The University of Georgia for all their help and the lessons they have taught me. I would like to thank Dr. Shan-Ho Tsai of The Georgia Advanced Computing Resource Center for her hard work and assistance. I would also like to thank all the individuals, from post doctoral member to undergraduate students, who have worked with me over the years for their incite and helping me to better my written and verbal communication skills so that I may share my work with the world. We would also like to thank Eric Suter (University of Georgia) and Kara Ponder (University of Georgia) for their individual contributions and hard work as well as Dr. Jason Galyardt, Dr. David Henley, and Dr. Kyujin Kwak for their assistance and contributions.

The software used in this work was in part developed by the DOE-supported ASC/Alliance Center for Astrophysical Thermonuclear Flashes at the University of Chicago. The simulations were performed at The Georgia Advanced Computing Resource Center (GACRC) of the University of Georgia. Figures were generated with a combination of IDL (Exelis Visual Information Solutions, Boulder, Colorado) and the yt analysis toolkit (Turk et al. 2011). This work was supported by NASA grants NNX00AD13G, NNX09AD13G, and NNH11ZDA001N-ATP, awarded through the Astrophysics Theory Program.

Table of Contents

List of Tables

List of Figures

Chapter 1

Introduction

High Velocity Clouds (HVCs) were first discovered in observations by Münch & Zirin (1961) by emission of neutral hydrogen (H I) at high velocity relative to the Local Standard of Rest (LSR). Classically HVCs are defined as clouds of H I with speeds that differ from the LSR by $|v_{LSR}| \geq 90$ km s^{-1} but speeds as low as 70 km s^{-1} and as high as 100 km s^{-1} have been used to define the lower boundary of the definition of an HVC (Wakker & van Woerden 1997, and references therein). This H I emission covers a large portion of the sky (see Putman et al. 2012, Figure 1) at a covering percentage of 37% with column densities exceeding $\sim 7 \times 10^{17}$ cm^{-2} (Murphy, Lockman, & Savage 1995; Lockman, Murphy, Petty-Powell, & Urick 2002). However, today we also define high velocity ionized material as HVC material and even moderately ionized high velocity material covers large percentages of the sky. For example, Si III covers 81% (Shull et al. 2009; Collins et al. 2009) and O VI covers 60% (Sembach et al. 2003) of the sky.

Spitzer (1956) suggested that these cool clouds of H I are in equilibrium with the hot (T$\sim 10^6$ K) Galactic halo. As HVCs move through their ambient environment, be it the Galactic halo or the intergalactic medium (IGM), the cloud material and ambient material interact through a variety of hydrodynamic processes. These processes include ablation, condensation, mixing, entrainment, etc. By modeling these interactions we can better understand the creation and lifetimes of HVCs as well as their effects on the Galaxy.

The origin theories of HVCs fall into three major categories; fountain (or feedback), satellite accretion, and IGM accretion. The fountain model (e.g., Shapiro & Field 1976; Bregman 1980) yields HVCs close to the Galactic disk ($z \leq 10$ kpc) by ejecting gas from

the disk via feed back processes like stellar winds and supernovae. This ejected material rises above the disk, cools, condenses, and can begin falling back towards the disk. Satellite accretion is exemplified by the Magellanic Stream. As the Large and Small Magellanic Clouds interact with the extended halo of the Milky Way material is ram pressure and tidally stripped from the galaxies and seen at high velocities in the LSR (see Wakker & van Woerden 1997; Putman et al. 2012). Accretion from the IGM occurs when material in intergalactic filaments cools and condenses. This material could begin to accelerate under the force of gravity towards the nearest galaxy and appear as a HVC. These types of clouds have been simulated by Joung et al. (2012) and observed between M31 and M33 by Wolfe, Lockman, & Pisano (2016). However, the observation of these clouds is a special case and the true origin of a HVC is rarely known.

Different origins create clouds from disparate reservoirs of gas with varying metallicities. For example, a cloud generated by a fountain will initially have a metallicity similar to the Galactic disk. A cloud generated via satellite stripping will have a metallicity comparable to the metallicity of the satellite (e.g., the Magellanic Stream CITE). Finally, a cloud that has condensed from the IGM, a primordial reservoir of gas, will have a low metallicity. As these clouds move through the ambient environment they will entrain ambient material which will augment their observed metallicities. By determining if there is a trend for how ambient material augments a cloud's metallicity we can determine the initial metallicity of a HVC and therefore the cloud's origin. For a detailed analysis of HVC mixing see Gritton et al. (2014) presented in Chapter 2.

HVCs also impact the chemical evolution and star formation rate (SFR) of the Galaxy. In a closed system, with no gas outflow or inflow, a galaxy in isolation will deplete the reservoir of cool star forming gas. Over time this depletion will result in lower SFRs. The current SFR of the Milky Way is between $\sim$1 and $\sim$3 $M_{\odot}$ yr^{-1} and has been constant over a long period of time (see Putman et al. 2012, and references therein). To account for this constant SFR the star forming disk of the Galaxy must have an external source of cool

gas. An additional problem is as stars die they pollute the surrounding gas with the metals they formed. In a closed system this should result in a monotonic rise in the metallicity of gas and stars in a galaxy over time. However, the metallicity of the Galaxy's star forming disk does not show the monotonic rise in metallicity one would expect from a closed box model. This problem is referred to as the G-Dwarf Problem (van den Bergh 1962; Pagel et al. 1979; Cowley 1995). In order for the star forming disk gas, and the stars generated from such gas, to maintain lower than expected metallicities over long periods of time there must be an inflow of cool low metallicity gas. Subsolar metallicity HVCs on trajectories that intersect the disk yield possible answers to both the question of maintained SFR and the G-Dwarf Problem. Low metallicity clouds should be generated by satellite stripping and IGM accretion but this presents its own complications. These clouds are formed in the extended halo and intergalactic space and must survive traversing the great distances to the disk.

One method to increase the lifetime of a HVC is to condense material from the ambient environment to increase the mass of the cloud or to reduce the net rate at which the cloud loses mass due to fragmentation and evaporation. By tracking the ambient material that cools and condenses into HVCs in hydrodynamic simulations we can determine if condensation has a non-negligible effect on the mass of a HVC. For a detailed analysis of condensation see Gritton et al. (2017) presented in Chapter 3

Because the evolution of a HVC is dependent upon the instabilities at the interface between the cloud and the ambient medium (see Kwak & Shelton 2010) we include a study of the effects of magnetic fields on the evolution of HVCs. It has been show by Chandrasekhar (1961), Miura (1984), and Malagoli et al. (1996) that magnetic fields can damp the instabilities of sheer flows. Magnetic fields can also effect the motions of fluids (Santillán et al. 1999; Raley et al. 2007; Kwak et al. 2009; Galyardt & Shelton 2016). Kwak et al. (2009) simulated 3-dimensional HVCs falling through a magnetized plasma in a fountain model. Fountain model clouds are normally smaller than HVCs produced through stripping of satellite galaxies and condensation of the IGM. We study the effects of magnetic fields on massive clouds

akin to those that would be generated via stripping or condensation of the IGM. We present our findings in Chapter 4.

Chapter 2

Mixing between High Velocity Clouds and the Galactic Halo[1]

[1]Gritton, Jeffrey A., Shelton, Robin L., and Kwak, Kyujin, 2014, *The Astrophysical Journal*, Vol. 795, No. 99. Reproduced by permission of the AAS

2.1 Introduction

High velocity clouds (HVCs) are clouds of gas whose speeds differ substantially from the local standard of rest (LSR). The minimum speed in the LSR reference frame is classically defined as $|v_{LSR}| = 90$ km s^{-1}, but it should be noted that speeds as low as 70 km s^{-1} and as high as 100 km s^{-1} have been used to define a lower limit for HVCs (Wakker & van Woerden 1997, and references therein). Although the original use of the term 'HVC' implied that the cloud is neutral, ionized high velocity material has been observed (see Hill et al. 2009 and Putman et al. 2012). In fact, moderately ionized and highly ionized fast moving material appears to cover larger fractions of the sky (81% for Si III, Shull et al. 2009; Collins et al. 2009 and 60% for O VI, Sembach et al. 2003) than does neutral material (37% for H I with column densities exceeding $\sim 7 \times 10^{17}$ cm^{-2}, Murphy et al. 1995; Lockman et al. 2002). For the purpose of this paper, we shall refer to both neutral and ionized high velocity gas as HVC gas.

Three major origin theories exist for HVCs; feedback (or fountain), satellite accretion, and accretion from the IGM. Feedback entails Galactic disk gas being ejected into the halo, like in a fountain that is energized by various processes such as stellar winds from young stars and supernovae. This ejected gas cools in the halo, via radiative cooling, and accretes onto the disk. The second idea on our list, the loss of material from satellite galaxies is exemplified by the Magellanic Stream (see Figure 1 of Wakker & van Woerden 1997 and Putman et al. (2012)) that trails behind the LMC and SMC. As these dwarf galaxies pass through the Milky Way's extended halo, some of their gas is ram pressure stripped and tidally stripped off of them. Perhaps as the gas falls towards the disk of our Galaxy it may become shock heated and fragment to the point of becoming indistinguishable from our Galaxy's halo gas or condense, due to radiative cooling, and continue to travel toward the disk of our Galaxy as HVCs. Lastly, dark matter-dominated gas-bearing clouds are both expected in simulations of the Local Group (Klypin et al. 1999) and observed (Adams et al. 2013) while IGM that flows along galactic filaments has been shown in simulations to condense and accrete along

the filaments (Joung et al. 2012). Some of this gas could continue to cool and begin falling towards our Galaxy's disk.

Each of these origins results from a different reservoir of gas, each of which should have a different metallicity. Thus observed metallicities provide clues to the origins of the clouds. For example, Tripp et al. (2003) and Collins et al. (2007) state that the low metallicities and differing metallicity measurements between different sight lines in Complex C imply that it originated from a more pristine reservoir of gas than the disk of the Milky Way and has mixed, and is mixing, with ambient material.

A cloud's metallicity, however, is also affected by the cloud's interaction with its environment. In our simulations, the HVC gas mixes with ambient halo material. Specifically, during the mixing process, the HVC fragments and the resulting fragments entrain and accelerate halo material. The metallicity of the mixed material is between that of the original cloud and the halo. As the cloud continues to move through the halo it will entrain more halo material, further modifying the observed metallicity.

It should be noted that, for the purpose of this paper, we do not use the technical definition of metallicity ($\log_{10}\left(\frac{n_\beta}{n_H}\right) - \log_{10}\left(\frac{n_\beta}{n_H}\right)_\odot$), where n_β is the number density of any chosen element, β, and n_H is the number density of hydrogen. In casual discussion, the term metallicity is taken to mean the ratio of the measured abundance over the solar abundance ($\frac{\left(\frac{n_\beta}{n_H}\right)}{\left(\frac{n_\beta}{n_H}\right)_\odot}$). We use this meaning of the term metallicity and use the $\left(\frac{n_\beta}{n_H}\right)_\odot$ values in Anders & Grevesse 1989; e.g., 9.77×10^{-2}, 3.63×10^{-4}, 1.21×10^{-4}, and 8.51×10^{-4} heliums, carbons, nitrogens, and oxygens per hydrogen. Our definition allows us to define solar metallicity to have a value of unity ($\mathcal{M}_\odot$=1.0). This shall be the convention used throughout the paper when discussing the effects of mixing upon the various metallicities we report, unless otherwise stated.

Not only is determining the extent of mixing important for determinations of a cloud's original metallicity, but it is also important for understanding the accretion of Milky Way gas into HVCs. To examine the effect of mixing in detail, we run detailed 2 and 3 dimensional

hydrodynamic simulations. We use the FLASH version 2.5 (Fryxell et al. 2000) code. Our methodology and initial conditions are described in Section 2.2. In Section 2.3, we present the simulational results. Specifically, Subsection 2.3.1 shows how the metallicity of high velocity material can be augmented on small scales. Subsection 2.3.2 shows that the degree of mixing is correlated with the ionization level of the gas such that weakly ionized high velocity gas is least mixed and highly ionized high velocity gas is well mixed. In Subsections 2.3.2.1 and 2.3.2.2, respectively, we explore the effects of mixing on the high velocity and decelerated gas. In Subsection 2.3.3 we further examine the relationship between velocity and metallicity. We present our conclusions in Section 2.4.

2.2 Numerical Code and Initial Parameters

We use FLASH to calculate the hydrodynamic interaction between the cloud and Milky Way halo gas. We implement two general domain geometries, one of which uses a 2 dimensional, fixed, cylindrically symmetric domain of height=20,800 pc (spanning from z=-1,200 pc to 19,600 pc) and radius=1,200 pc (Model A), while the other (Model B) uses a 3 dimensional, fixed, Cartesian domain of height=10,800 pc in z (spanning from z=-1,200 pc to 9,600 pc) and cross sectional dimensions x=1,200 pc and y=1,200 pc (spanning from x=0 pc to x=1,200 pc and y=0 pc to y=1,200 pc). In Model B we assume a nearly symmetric structure across the x=0 pc and y=0 pc planes and therefore simulate one fourth of the cloud to make better use of our computational resources. In addition to the $\frac{1}{4}$ cloud results presented in this paper, preliminary simulations of a half-cloud were made. There was little difference in visible morphology between the $\frac{1}{2}$ cloud and $\frac{1}{4}$ cloud simulations. However, additional half-cloud simulations were deemed unfeasible due to their longer wall clock times. We reserve half-cloud simulations for future projects. Although we use an adaptively refinable grid, we begin the simulations at full refinement such that all zones span $\sim$3 pc along the z-direction and $\sim$3 pc along the radial direction for Model A, and $\sim$9 pc in x, y, and z directions for

Model B. Aside from the domain and geometry, all other initial parameters are the same between our two models.

A 150 pc radius spherical cloud is initially placed with its center at z=0 pc, r=0 pc in Model A, and at x=0 pc, y=0 pc, and z=0 pc in Model B. As in Model C of Kwak et al. (2011), all of our model clouds are warm (cloud temperature, T_{cl}=10^3 K), moderately dense (cloud density of hydrogen, $n_{H,cl}$=0.1 cm^{-3} and density of helium, $n_{He,cl} \cong 0.1 \times n_{H,cl}$) and surrounded by hot (T_{ISM}=10^6 K), low density (density of hydrogen, $n_{H,ISM}$=10^{-4} cm^{-3} and density of helium, $n_{He,ISM}$= $0.1 \times n_{H,ISM}$) Milky Way halo gas. The halo number density falls within observational constraints (see Kwak et al. 2011). It is slightly less dense than the material around Complex C ($10^{-3.3}$ to $10^{-3.0}$ cm^{-3}, see Hsu et al. 2011) and similar to that around the tail of the Magellanic Stream ($10^{-4.1}$ to $10^{-3.7}$ cm^{-3}, see Hsu et al. 2011). Our halo density is chosen to mimic the extended halo as calculated by Wolfire et al. (1995) and modeled by Heitsch & Putman (2009). Our halo material remains at a constant density throughout the simulation. This is not so dissimilar from reality, in that the observationally determined gradient is small, with a factor of $\sim$6 decrease in density from the height of Complex C to the height of the tail of the Magellanic Stream. An object travelling at an oblique angle to the Galactic disk would experience an even smaller gradient. We choose this scenario so that the effects of mixing can be studied over a longer period of simulated time without changes to variables, such as ambient density, that would effect the rates of ablation by damping or increasing hydrodynamic instabilities. We did not model density inhomogeneities (i.e., clumpiness) as the size scale and density contrast of such inhomogeneities are not well understood. Future projects shall focus on the effects of density, speed, magnetic fields, and gravity, as they relate to the survival and mixing of HVCs. Each of these variables can play important roles in the evolution of an HVC and may alter the mixing characteristics (see Kwak et al. 2009).

Rather than model a sharp boundary between the cloud and ISM, we model a smooth transition in both density and temperature following the function

$$n_H\,(r) = -0.5\,(n_{\rm H,\ cl} - n_{\rm H,\ ISM})\tanh\left(\frac{r - 150{\rm pc}}{20{\rm pc}}\right) + 0.5\,(n_{\rm H,\ cl} + n_{\rm H,\ ISM})$$

which is similar to the density profiles used in simulations by Heitsch & Putman (2009) and Kwak et al. (2011) who based their hyperbolic tangent transition function on the observations of Burton et al. (2001). For a graphical representation of the above equation see Figure 1 of Kwak et al. (2011). The density decreases with radius in a transition zone that extends from $r \cong 90$ pc to $r \cong 210$ pc, with the above quoted cloud radius being the radius at which the density drops to half that of the cloud's center. Any material within the transition zone that initially has $n_H \geq 5\ n_{H,ISM}$ (i.e., any material within ∼210 pc of the cloud's center) is assigned the velocity and metallicity of the cloud (see below); note that the majority of this material (over 80% by mass) is within r=150 pc. At the beginning of each simulation, the temperature in the transition zone increases with radius as the density decreases with radius such that the thermal pressure remains constant and is equal to that in the cloud and ambient gas at the beginning of the simulation. It should be noted that the pressure used in the hydrodynamic calculations is determined using the approximation that the hydrogen and helium in the cloud are fully ionized, but collisionally ionized gas at the model cloud temperature is not fully ionized. The ionization approximation affects only the pressure calculations done by FLASH. The effect of this approximation is that the cloud is less compressible than a fully neutral cloud. However, observed clouds are found to be partially ionized. Hill et al. (2009), for example, determined the mass of the Smith Cloud to be 5.0×10^6 solar masses ($M_\odot$) in neutral hydrogen and $\sim3\times10^6\ M_\odot$ in ionized hydrogen. From this we can say that $\sim \frac{3}{8}$ of the hydrogen in the Smith Cloud is ionized.

The metallicities of observed HVCs are generally lower than those of the Milky Way and may have been even lower before the high velocity gas began to mix with the Milky Way

gas. In order to track the permeation of Milky Way gas into high velocity gas and vice versa, we give our model HVC and model halo gas different metallicities. We give the halo gas solar photospheric metallicities ($\mathcal{M}_h$=$\mathcal{M}_\odot$=1.0) and we give the HVC gas, also simply referred to as cloud gas, extremely small metallicities, $\mathcal{M}_{cl}$=0.001. The low metallicity of the cloud extends through most of the transition zone and ends where $n_H = 5\ n_{H,ISM}$. Later in the simulation, when moderate metallicities of metals are found in high velocity gas, their magnitudes minus the initial 0.001 metallicity of the cloud, can be attributed to mixing and thus directly provide a quantitative measure of the permeation of Milky Way gas into high velocity cloud gas. It should be noted that our choices of metallicities for the initial cloud and ambient material can be changed to any value.

As will be shown in Section 2.3, the degree of permeation varies such that plasma in which the metals are highly ionized generally contains larger fractions of Milky Way gas than does plasma in which the metals are poorly ionized. Examination of this trend requires accurate tracking of the ionization levels of the gas, for which we use FLASH's non-equilibrium ionization (NEI) module. The NEI module is used to calculate the extent of the ionization and recombination that occurs during each time step, although the ionization levels at the beginning of each simulation are calculated under the assumption of collisional ionization equilibrium. Thus initially the cloud is predominantly neutral, based upon its temperature.

As in Model C of Kwak et al. (2011), the halo gas and the HVC move at 150 km s^{-1} relative to each other. A velocity of this magnitude allows us to distinguish high velocity material from normal velocity material. Our simulations are conducted in the initial rest frame of the cloud. I.e., at the beginning of the simulation the cloud is stationary in the domain and throughout the simulation hot halo gas flows upwards (in the positive z-direction) at a speed of 150 km s^{-1}. This choice of rest frame allows us to model the mixed gas over a longer period of time in a moderately tall domain than could be done if the simulations had been conducted in the halo's rest frame. However, for the convenience of the reader, and for easier comparison with observations, we report all velocities in the halo's rest frame, from the point

of view of an imaginary observer situated below the bottom of the domain. We accomplish the conversion by subtracting 150 km s^{-1} from the simulated velocities in the z-direction. Henceforth, simulated material that moves upwards (away from the Galactic plane) in the halo's rest frame will be described as having a positive velocity in the z-direction while material that moves downwards (toward the Galactic plane) will be described as having a negative velocity. The total duration of our simulations is 200 Myrs in simulational time which is longer than is typical in HVC simulations. This duration and all initial parameters are listed in Table 2.1.

2.3 Results

The HVC's behavior; including its deformation, shredding, and mixing with the surrounding gas, can be seen in Figure 2.1 for Model B (Model A exhibits similar gross behavior). The top row of panels in the figure shows the density in the form of number of hydrogens per cm^3, where, as mentioned in Section 2.2, there are also 9.77×10^{-2} heliums for every hydrogen. The middle row shows the temperature. The bottom row shows the metallicity, where oxygen is used as an example element though we also simulate and track carbon. Each variable is plotted as a function of location on the x-z plane along a slice through the domain at y=0. We assume that the structure is approximately symmetric across the x=0 pc and y=0 pc plane; only positive x and y space is simulated, and only one slice at y=0 pc is shown. The displayed panels depict the structure at 0, 40, 80, 120, 160 and 200 Myrs of simulation time but data is collected via output files every 2 Myrs of simulation time and a large number of timesteps (typically 560 and 90 for Models A and B) occur between file outputs.

The semicircle shaped object initially at x, z=0 in the leftmost of these panels is a slice of one quarter of the cloud at the beginning of the simulation. As time progresses, the ISM sweeps past it, deforming its shape, creating instabilities, and pulling off material. In the region above the cloud, the two fluids (ablated cloud material and ISM) create a plume of intermediate density material that is observable in the density profiles in the top row of

Figure 2.1. The ablated cloud material and ambient materials mix, not only on the large scale (such as the 150 pc radius of the cloud), but also on the small scale (in the simulations we see mixing on scales as small as a few cells). The mixing of ablated cloud gas with halo gas lowers the temperature of the plume material relative to that of the halo, and radiative cooling lowers it further. These processes, mixing and radiative cooling, cause the plume of ablated and mixed gas that trails the cloud to be cooler than its surroundings. See the temperature profiles in the center row of Figure 2.1. In general the metallicity in the plume is greatest at the top and least at the bottom. While this is also the case for the temperature, temperature and metallicity are not tightly correlated. The metallicity of any given segment of gas is affected only by mixing while the temperature of any given segment of gas is affected by mixing and cooling. The cooling rate is dependent upon the temperature of the mixture and is generally different from the weighted mean of the temperature dependent cooling rates of the mixing gasses.

Not only are the metallicities in the mixed gas interesting for observational studies, but in our simulations they provide a quantitative measurement of the extent of mixing that has occurred. A mixture in which the fraction (by mass) of cloud material is f_{cl} and the fraction (by mass) of halo gas is f_h will have an average metallicity of $\mathcal{M}{=}f_{cl}\mathcal{M}_{cl}+f_h\mathcal{M}_h$ where $\mathcal{M}_{\rm cl}$ and $\mathcal{M}_{\rm h}$ are the initial metallicities of the cloud and halo respectively. We choose our initial metallicities so that the preceding equation simplifies to $\mathcal{M}\cong f_h$, allowing us to track both the mixing of cloud and halo gas and the evolution of the cloud's metallicity simultaneously.

2.3.1 Example Fragment

As a demonstration, we examine the mixing in a single intermediate temperature, intermediate density ablated fragment modeled in the FLASH simulation for Model A. We choose a somewhat dense fragment of material that was ablated from the cloud. Figure 2.2a identifies the chosen fragment at 80 Myrs when it is located at (r, z) = (350 pc, 1,000 pc); Figure 2.2b shows a close-up view of the fragment at this time. We track the fragment's motion as the

simulation time progresses by an additional 10 Myrs. Figures 2.2 c&d show the fragment at 90 Myrs, after it has reached a position of (r, z)=(350 pc, 1,900 pc). In order to provide an example quantitative analysis, single parcels in the densest part of the fragment are chosen for examination at both epochs. These parcels are located in the centers of the red boxes in the close-up images. We determine the extent of the mixing that has occurred in these parcels by examining their metallicities. At 80 Myrs the center parcel has an oxygen metallicity of 5% of the solar value, and using $\mathcal{M}= f_{cl}\mathcal{M}_{cl} + f_h\mathcal{M}_h$ from the paragraph above, as well as $\mathcal{M}_{\rm cl}$=0.001 and $\mathcal{M}_{\rm h}$=1.0, we deduce that the parcel is composed of 5% halo gas and 95% cloud gas. In the span of 10 Myrs, the metallicity in the center of the fragment increases to 10% of the solar value, indicating that the material in the fragment's center is now composed of 10% halo material and 90% cloud material. Therefore we can state that some halo gas permeates even moderately dense tails of ablated gas, and that the timescale for permeation is relatively short. These points apply to all of our simulations.

2.3.2 Global Analysis

Logically, the extent of mixing should be related to the duration of exposure between the material that has been ablated from the cloud and the surrounding hot halo gas. There should also be a relationship between the degree of mixing and the material's ionization level. This is because mixing transfers thermal energy from the halo material to the cloud material, bringing the temperature of the mixed gas to an intermediate value. As the temperature begins to equilibrate, the atoms that were contributed by the cloud should begin to ionize while those that were contributed by the halo should begin to recombine. Subsequent radiative cooling only complicates the situation. The hydrodynamical interaction slows the material that was contributed by the cloud while accelerating the entrained halo material, resulting in a relationship between the material's velocity and its degree of mixing (and thus its metallicity). In this subsection, we calculate the progression of mixing for gas throughout the domain as a function of time, ionization level, and velocity. We characterize the mix-

ing by the resulting metallicity of our sample elements oxygen and carbon and present our results in a form that can be compared with observations.

A real observation of a high velocity cloud will sample material along a line of sight. Optimally, multiple lines of sight will be used in order to calculate the average metallicity. In both cases, the metallicities of various parts of the structure are averaged together. Similarly, averages can be calculated from our simulation. Here, we average over all of the gas in the domain that has a low speed relative to the halo ($\vec{v_z}$ <100 km s^{-1}), and we separately average over all of the gas in the domain that has a high speed relative to the halo ($\vec{v_z} \geq 100$ km s^{-1}). These procedures are equivalent to calculating the averages from hundreds of vertical sight lines through the domain. Thus, when we examine the extent of the mixing as sampled by particular ions of oxygen and carbon, we do so for all such ions in the domain; i.e. we average the metallicities of all such ions in the domain.

We plot the average metallicities (i.e., the metallicity of oxygen averaged over all parcels in the domain), $\bar{\mathcal{M}}$, with the appropriate velocity in the domain, as functions of time for individual ionization levels of oxygen for each model in Figure 2.3. We show the metallicities of both high velocity, $\bar{\mathcal{M}}_{v>100}$, and low velocity, $\bar{\mathcal{M}}_{v<100}$, material. The latter includes the 'stationary' halo gas, which outweighs the cloud gas. Here, we treat $\bar{\mathcal{M}}$ as being equal to f_h, because, for our choices of cloud and halo metallicities, they are approximately equal. The same can be stated for the carbon traces in both models. Additionally, certain ions of carbon follow the same trends as an oxygen counterpart which we shall discuss in the following subsections. Therefore, for clarity, our plot of the metallicity as traced by ions of carbon uses a single model, Model B (see Figure 2.4).

2.3.2.1 Analysis of High Velocity Gas

We first consider the high velocity O I panel of Figure 2.3. At the start of the simulation, the only source of high velocity gas in the domain is the cloud, including most of the transition zone between the cloud's interior and the halo. Initially the cloud has approximately

primordial metallicities. For this reason, the initial metallicities of the O I to O IX ions in the high velocity gas is $\mathcal{M}_{cl}$=0.001. As the simulation progresses, hot, highly ionized, solar metallicity, halo plasma mixes with material at the surface of the cloud and with material that has been shed from the cloud, rapidly augmenting the average metallicities in the formerly-cloud gas. Early in the simulations, most of this material moves at $\vec{v_z}$ >100 km s^{-1}, in which case, the entrained metals count toward $\bar{\mathcal{M}}_{v>100}$ rather than $\bar{\mathcal{M}}_{v<100}$. Although the freshly entrained halo gas had been hot, it cools by sharing thermal energy with the formerly-cloud gas and by radiating photons. As the metals in the entrained halo ions cool, they recombine, causing $\bar{\mathcal{M}}_{v>100}$ for O I to rise approximately monotonically throughout the simulation. By the end of the simulation, $\bar{\mathcal{M}}_{v>100}$ for O I for Model A has reached a value slightly greater than 0.1 while in Model B has risen to over 0.25. Thus, even the neutral part of the HVC contains ∼10% or ∼25% halo gas in Models A and B respectively.

The difference between $\bar{\mathcal{M}}_{v>100}$ for these two cases shows that the 3D simulations are more efficient than the 2D simulations at entraining and cooling halo material. This is because the clumps are able to fragment along all three Cartesian dimensions in the 3D simulations but are able to fragment along only 2 dimensions (r,z) in Model A. Model B is the more realistic of the two models.

For O II, O III, O IV, O V, and O VI, $\bar{\mathcal{M}}_{v>100}$ experiences a rapid increase during the first few timesteps as halo material mixes with the outermost portions of the cloud. The lower density at the interface between the cloud and halo material allows this gas to be ablated and mixed more efficiently. But soon the behaviors of $\bar{\mathcal{M}}_{v>100}$ for these ions becomes more complicated. Ionization of former cloud gas reduces $\bar{\mathcal{M}}_{v>100}$ while recombination of entrained, initially highly ionized halo gas raises $\bar{\mathcal{M}}_{v>100}$ with the result that $\bar{\mathcal{M}}_{v>100}$ vacillates in time about a near constant value when the cloud is stable and increases to higher values during ablation events. $\bar{\mathcal{M}}_{v>100}$ for O II O III, O IV, O V, and O VI reach values values of ∼0.2 to ∼0.6.

O VII, O VIII, and O IX are the natural charge states of oxygen in the halo gas. The high velocity O VII, O VIII, and O IX ions that appear from the second timestep onwards in our simulations are due to halo material that has been accelerated by the cloud. In Model A, $\bar{\mathcal{M}}_{v>100}$ for these ions asymptotically approaches about 0.9. In Model B, $\bar{\mathcal{M}}_{v>100}$ for these ions is more complicated. The values rise early on, fall, and later reach a maximum value around 0.7.

The above noted details notwithstanding, the trends in metallicities are often fairly similar in Models A and B and all values agree to within an order of magnitude. However, of the two models, Model B has the more realistic simulation geometry and will be relied upon more heavily in subsequent subsections. The above comparisons also show that the shortness of Model B's domain (which allows mixed material to flow out of the domain through the upper boundary as early as t=30 Myrs) does not greatly affect the $\bar{\mathcal{M}}_{v>100}$ results. Most of the material that has left Model B's domains had slowed significantly before doing so and is therefore not considered in our calculation of $\mathcal{M}_{v>100}$.

We plot $\bar{\mathcal{M}}$ values for carbon in Figure 2.4. Unlike Figure 2.3 we only plot Model B. Ions that mimic each other's trends are as follows: O I and C I, O II and C II, O III and C III, O IV and C IV. Note that O V and O VI match C V, with values varying by no more than 0.05 between O VI and C V. All of the remaining ions, O VII, O VIII, O IX, C VI, and C VII, follow the same trend with values increasing in the order C VI, O VII, C VII, O VIII, O IX.

For the majority of the ions of both carbon and oxygen, the average metallicity in the high velocity gas in our simulations is generally at least 300 times larger than the original metallicity of the cloud, which in our simulations is extremely low.

Initially Model B's domain (because of the symmetry, this represents $\frac{1}{4}$ of the cloud and surrounding halo) contains almost 13,000 $M_{\odot}$ of material at HVC speeds. Of this HVC gas 97% can be defined as cool (T$\leq 10^4$ K). As hot halo gas sweeps past the cloud, material is ablated from the cloud and mixed, resulting in intermediate temperatures, speeds, and metallicities. By 100 Myrs we see that the total mass of high velocity material in the domain

has increased by ∼40 solar masses due to capture of halo material and condensation. All of the gas at high velocities is counted, because the only material that leaves the domain has decelerated to velocities below 100 km s^{-1} and is no longer considered high velocity material. Of the high velocity gas 92% is cool while 8% is now warm or hot at 100 Myrs, showing that the evolution of the cloud happens slowly at first. As of 200 Myrs, the domain contains only about 3400 $M_{\odot}$ of high velocity material, $\sim \frac{1}{4}$ of the initial high velocity content, with ∼2600 $M_{\odot}$ as cool high velocity gas and ∼800 $M_{\odot}$ as warm or hot high velocity gas. I.e., in the span of 200 Myrs, $\frac{3}{4}$ of the initially high velocity gas has decelerated to speeds below 100 km s^{-1}.

2.3.2.2 Analysis of Low Velocity Gas

When we shift our attention to the low velocity gas, we see higher average metallicities in both carbon and oxygen. This effect occurs because the low velocity cut preferentially selects halo gas whose metallicities have been tempered by the addition of gas that has been ablated from the cloud and decelerated to within 100 km s^{-1} of the halo's rest frame. The contribution of the low metallicity cloud gas is most manifest in the O I and C I ions, because the original cloud was predominantly neutral while the original halo gas was nearly devoid of neutral material (with the exception of the cloud-halo interface, which includes a small amount of T≤T_{ISM} gas that has halo metallicity and halo velocity; this material is responsible for the solar metallicity low and intermediate ions in the domain at t=0 Myrs seen in Figure 2.3). For example, the value of $\bar{\mathcal{M}}_{v<100}$ for O I falls as low as 0.05 (before rising to higher values), which is the lowest $\bar{\mathcal{M}}_{v<100}$ for any of the ions in our simulations, while the value of $\bar{\mathcal{M}}_{v<100}$ for C I falls to 0.1 before rising. The presence of low and moderate metallicity O I and C I-bearing gas at $\vec{v_z}$ <100 km $^{-1}$ suggests that if low metallicity, low velocity gas is found in the halo, shredding of low metallicity HVCs is one possible source.

Mixing between the halo and cloud gas raises the temperature and ionizes formerly cloud gas by the time it has decelerated to a speed below 100 km s^{-1}. As the neutral material in the

slowed gas experiences warmer temperatures and collisions with faster electrons, it ionizes. This occurs as early as the first simulated timestep and results in significant changes to the metallicities of O II, O III, and O IV as well as C II, C III, and C IV, by the end of the first timestep. Thus $\bar{\mathcal{M}}_{v<100}$ for O II and O III as well as C II and C III, drop to less than 0.1, and $\bar{\mathcal{M}}_{v<100}$ for O IV drops to less than 0.3 within a few million years of the simulation's start. As we look at more highly ionized material the metallicities of O V and C IV are lowered less drastically but still experience values less than solar. After these initial drops, the $\bar{\mathcal{M}}_{v<100}$ for O II through O V, and C II through C IV, rise and fall with time, due to competition between ionization in the mixed, initially low metallicity cloud gas and recombination in the initially high metallicity halo gas. Thus, after the first million years, $\bar{\mathcal{M}}_{v<100}$ vacillates between smaller ranges: 0.08 to 0.5, 0.1 to 0.5, 0.2 to 0.5, and 0.3 to 0.7 for O II, O III, O IV, and O V respectively and similar values for C II through C V.

As we consider higher ionization states, we see preferentially more of the influence of the halo gas. Nearly all of the low velocity C V, C VI, C VII, O VII, O VIII, and O IX originates in halo gas, which has solar metallicity. Only a small fraction of these ions originate in ablated cloud gas that has merged with the halo gas. Thus, the gas contributed by the cloud only marginally lowers $\bar{\mathcal{M}}_{v<100}$ for these ions.

2.3.3 Velocity Selections

These trends raise the questions of whether or not clear relationships between metallicity and velocity would be predicted and could be seen throughout an HVC cloud or complex. In order to address the first of those issues, we have subdivided our previous velocity regimes into a larger number of regimes and replotted the metallicity as a function of time for 3 sample ions (O I, O V and O VIII) in Model B. The results are plotted in Figure 2.5. Note that the lowest velocity range excluded stationary halo gas. Also note that our highest velocity range ($v_z \geq 150$ km s^{-1}) samples the very small amount of gas in the domain that moves downwards faster than the cloud. Such gas resides in the portions of eddies that move

downward relative to the cloud's rest frame. Because of this gas's behavior, the $v_z \geq 150$ km s^{-1} curves are sporadic and unusual.

The other curves follow the trend that slower (from the point of view of an observer) gas is usually more metal-rich than faster gas. The degree of metal enhancement can change as a function of time; for the first 140 Myrs the trend can be seen in all 3 sampled ions.

With the exception of the $v_z \geq 150$ km s^{-1} curve, the metallicity tends to increase with decreasing gas velocity (from the point of view of an observer) for the first 140 Myrs. This shows the tight link between mixing and deceleration as both happen simultaneously after gas is ablated from the head of the cloud. After 140 Myrs, some of the velocity curves overlap. In order to determine if this relationship between speed and metallicity is observed in real HVCs, more data for more ions and along more sight lines are required.

2.4 Conclusion

In this paper we present FLASH simulations of HVCs traveling through low density gas in the outer halo. Very early in each simulation, hydrodynamic interactions begin to ablate material from the cloud. The ablated material falls behind the main body of the cloud, where it begins to create a tail. As additional material sheds from the cloud and decelerates, the tail grows, reaching a length of several kpc within the 200 Myrs of simulational time. Although a velocity gradient develops from the main body of the cloud (the head in a "head-tail" structure) through the tail of shed gas, some of the tail gas still travels at speeds ≥ 100 km s^{-1} and thus is fast enough to meet the definition of high velocity gas. Conversely, if the cloud has a higher metallicity than the halo, mixing would dilute the metal content of the cloud as it traveled toward the disk or orbited the galaxy.

Mixing between cloud gas and ambient gas occurs along the entire length of the head-tail structure. But, the tail gas, which has been exposed to the ambient gas for the greatest length of time, is most highly mixed while the head is least mixed. Not only does mixing take the form of the shredding and deceleration of cloud gas, but it is also involves the

entrainment and acceleration of halo gas. Thus, mixing boosts the metallicity of HVCs whose original metallicity was lower than that in the halo.

At any given time, the metallicity of the gas in any given cell in the domain is directly related to the fractions of material that have come from the halo and cloud, respectively. Thus, the metallicity of the gas can be seen as both a function of mixing and a tracer of previous mixing. Using FLASH hydrodynamic simulations, we estimate and present the degree of mixing as a function of time. We do this separately for the high velocity material and the low velocity material. We use oxygen and carbon as sample elements and present the mixing fractions and resulting metallicities as functions of the time-dependent ionization states of the oxygen and carbon atoms. Although in our simulations the original metallicity of the cloud is very low and the metallicity of the halo is much higher, we present an equation that can be used to determine the metallicity and degree of mixing in cases where the cloud and halo metallicities differ from those chosen for our particular simulations.

In order to more accurately predict the chemical evolution of any HVC, simulations specifically tailored to that cloud would be required. However, our simulations can make rough estimates for observed clouds. In our simulations, mixing raises the metallicity in the least ionized high velocity material from 0.1% to $\sim$ 25% of solar while raising the metallicity of the most ionized high velocity material from 0.1% to 70% of solar for Model B, our 3-dimensional model, over the span of 200 Myrs. Observations of high velocity neutral and once ionized gas in Complex A for example show that this complex currently has subsolar metallicity in O I ranging between 5% to 10% of solar (see Wakker 2001, Subsection 4.1). Furthermore, Complex C has also been shown to have subsolar metallicity using O I and Si I ranging between 10% and 30% of solar (Shull et al. 2011). If these two HVCs had been interacting with a solar metallicity halo for 200 Myrs all O I in Complex A and as much as 25% of the O I in Complex C could be due to halo material that has been mixed into the clouds as the clouds traveled through the Galaxy's halo. If an observer were to take the observationally determined metallicity (for example 30% of solar) and subtract off

the contribution due to mixing with halo gas over a period of 200 Myrs, (∼25% of solar), then the difference (up to 5% of solar) would be attributed to the cloud as it was before undergoing 200 Myrs of mixing. Such a small metallicity supports the suggestion that some HVCs originated in nearly primordial gas outside of the Galaxy. These are very rough estimates that would be improved upon by more pointed simulational studies whose purpose is to model these particular clouds. The metallicity of the ambient material could also be adjusted. If the halo were given subsolar metallicity the rate of metal augmentation would decrease. This would in turn mean primordial gas entering our halo would require more time traversing our halo to reach observed metallicities.

The simulational results also suggest that if an HVC is observed to have an extremely low metallicity then it must either be located far from a galaxy or have only recently entered that galaxy's metal rich halo.

Over the 200 Myrs of simulated time, parts of the cloud are ablated, decelerated, and/or mixed with hot halo gas. By the end of the simulation only about 21% of the amount of initially cool high velocity gas is still cool and traveling with a high velocity in the simulational domain, whereas the rest has either been heated via mixing with ambient material, such that this gas would no longer be defined as cool or has decelerated to the point we no longer define it as HVC material and would now define it as intermediate or low velocity gas. Considering that the simulations show that some ablated material decelerates to non-HVC velocities, much like in the simulations of Heitsch & Putman (2009) and Marinacci et al. (2010), we suggest that observations of low metallicities in intermediate and low velocity halo gas may indicate material that has been shed by an HVC.

We find that ablated and decelerated material tends to have undergone more mixing and have higher metallicities than its faster counterparts more recently shed from the main body of the cloud. This is most apparent during the first 140 Myrs of the simulation in all ionization states of oxygen. More observations along more sight lines with greater ranges of speed are required to determine if this relationship is observed in real HVCs.

Table 2.1: Initial Simulation Parameters

Model		
	A	B
Domain		
Coordinates	r,z	x,y,z
Geometry	Cylindrical	Cartesian
Symmetries	About z=0 pc	Across x=0 pc Across y=0 pc
Physical Size	0 pc $\leq$ r $\leq$ 1200 pc	0 pc $\leq$ x $\leq$ 1200 pc 0 pc $\leq$ y $\leq$ 1200 pc
	-1,200 pc $\leq$ z $\leq$ 19,600 pc	-1,200 pc $\leq$ z $\leq$ 9,600 pc
Simulation Duration	200 Myrs	
Cloud		
Initial Location	z=0 pc, r=0 pc	x=0 pc, y=0 pc, z=0 pc
Radius	150 pc	
Internal Density	Hydrogen: $n_{H,cl}$=0.1 cm^{-3} Helium: 0.1 $n_{H,cl}$	
Internal Temperature	$T_{cl}=10^3$ K	
Internal Metallicity	$\mathcal{M}_{cl}$=0.001	
Milky Way Gas		
Density	Hydrogen: $n_{H,ISM}=10^{-4}$ cm^{-3} Helium: 0.1 $n_{H,ISM}$	
Temperature	$T_{ISM}=10^6$ K	
Metallicity	$\mathcal{M}_h$=1.0	
Motion		
Speed	150 km s^{-1}	
Simulational Rest Frame	Initial cloud's rest frame	
Analysis Rest Frame	Halo's rest frame	

From top to bottom: domain parameters, initial cloud parameters, initial halo material parameters, simulated motion within the system, and assumed ionization fraction used in the calculation of the cooling rate in the low temperature gas.

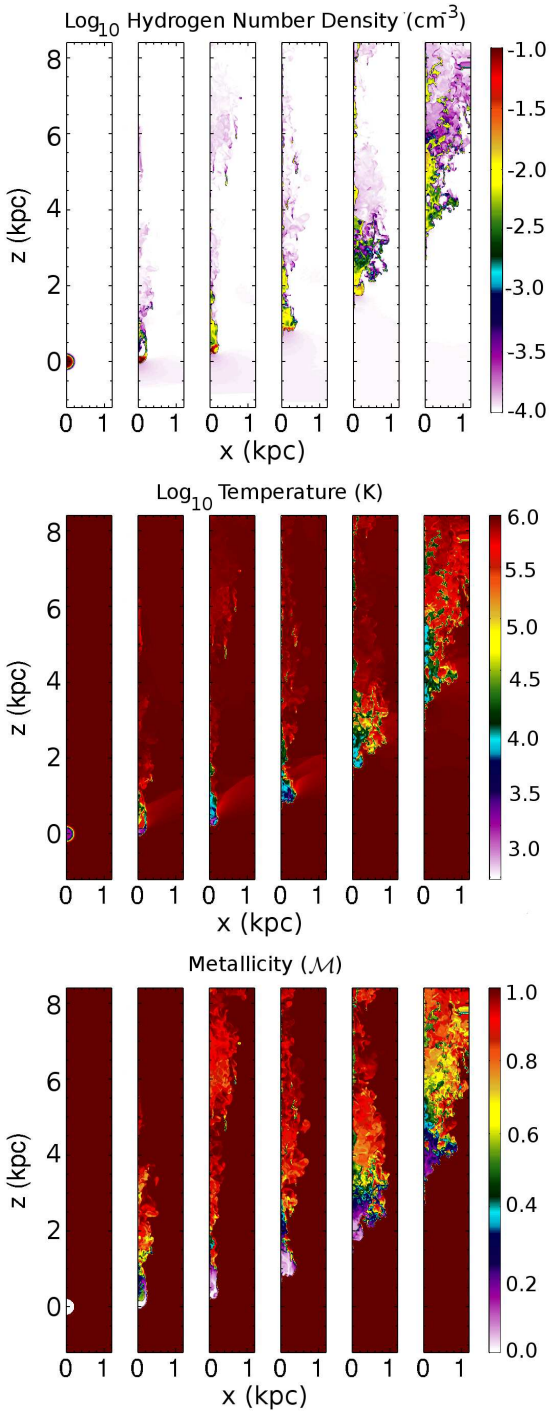

Figure 2.1: System Evolution

Plots of $\log_{10}$ hydrogen number density (in units of cm^{-3}, top row), $\log_{10}$ temperature (in units of K, middle row), and oxygen metallicity (bottom row) are presented for Model B. Each image is from a single 2 dimensional cut, along y=0. The model is shown at a series of ages (0, 40, 80, 120, 160, and 200 Myrs) from left to right, thus revealing the evolution of the system over time.

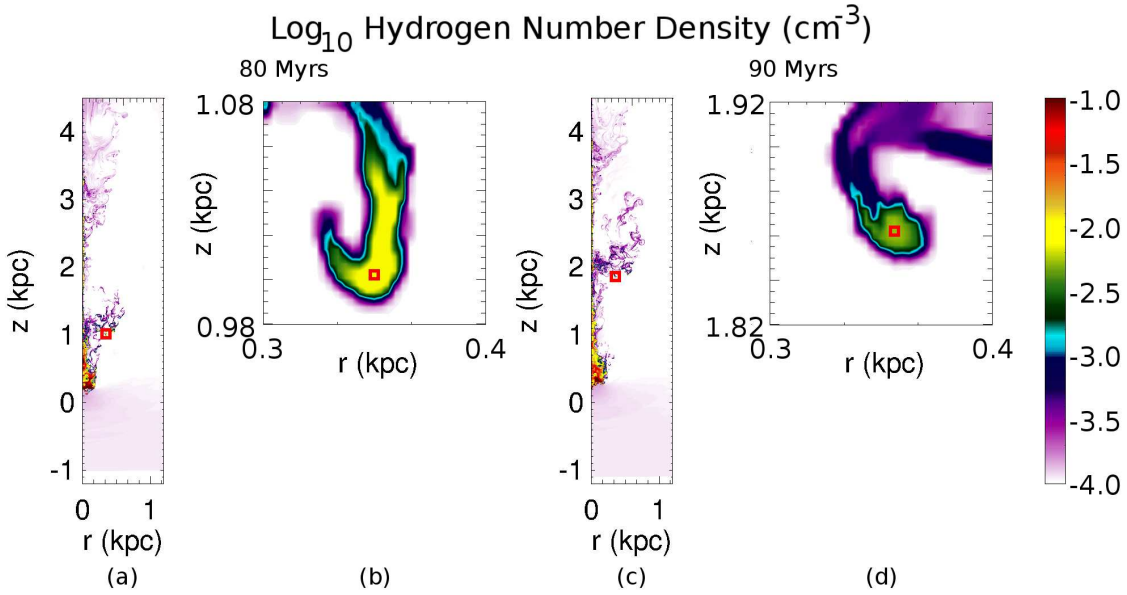

Figure 2.2: Quantitative Example Fragment

Plots of $\log_{10}$ hydrogen number density for Model A showing the fragment used in our quantitative example. The left images, a&b, show the simulation at the age of 80 Myrs, while the right images c&d show the simulation at the age of 90 Myrs. Images a&c show the entire domain with the red square identifying and centered on the chosen fragment. Images b&d are close-up images of the fragment. The red squares in panels b and d are centered on cells chosen for our example quantitative analysis in Section 2.3.1.

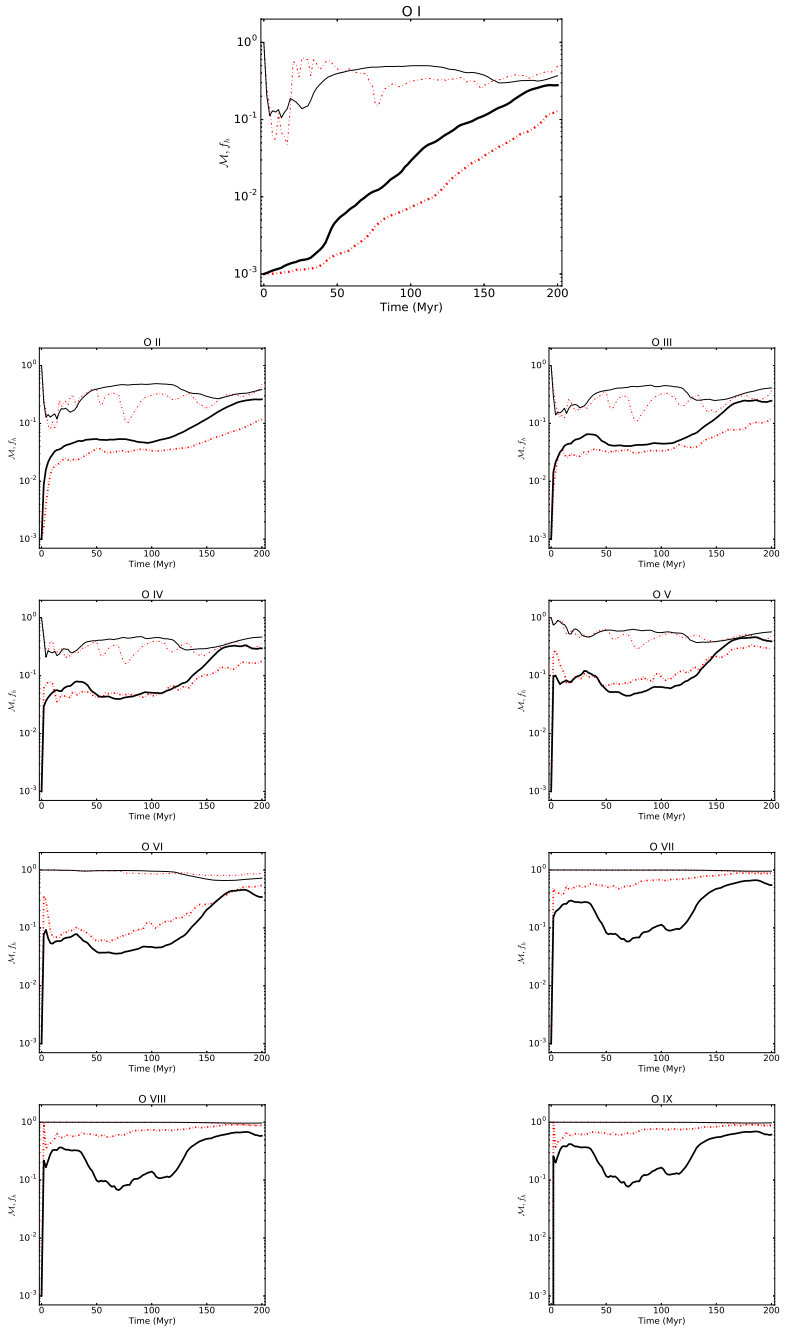

Figure 2.3: f_h vs. Time

Average metallicity ($\bar{\mathcal{M}}$) and halo gas fractions (f_h) as functions of time for each ionization state of oxygen. Model A is represented by the red dot-dash line while Model B is represented by the solid black line. High velocity material for each model is represented by the thicker lines and low velocity material by the thinner counterpart.

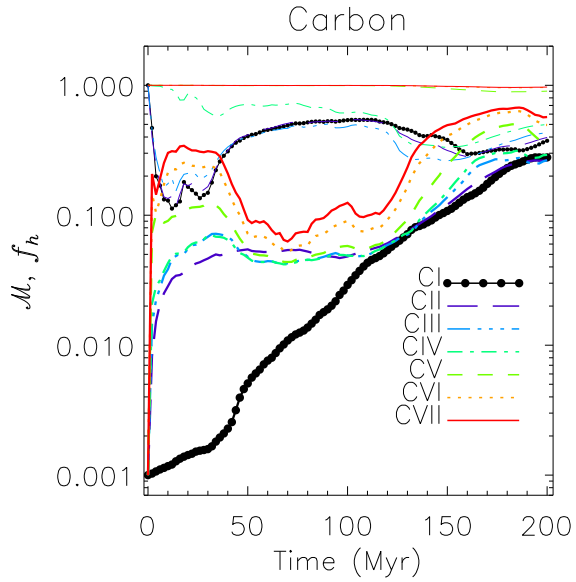

Figure 2.4: $\bar{\mathcal{M}}$ vs. Time & f_h vs. Time

Average metallicity ($\bar{\mathcal{M}}$) and halo gas fraction (f_h) as functions of time for each ionization state of carbon. Only Model B is plotted as all models mimic the trends of oxygen with values agreeing within 0.050. HVC material is plotted using thicker lines while the low velocity material is plotted using the thinner counterparts. Individual ionization states are plotted using different shades from black to light gray (different colors in the online version) and with varying line styles.

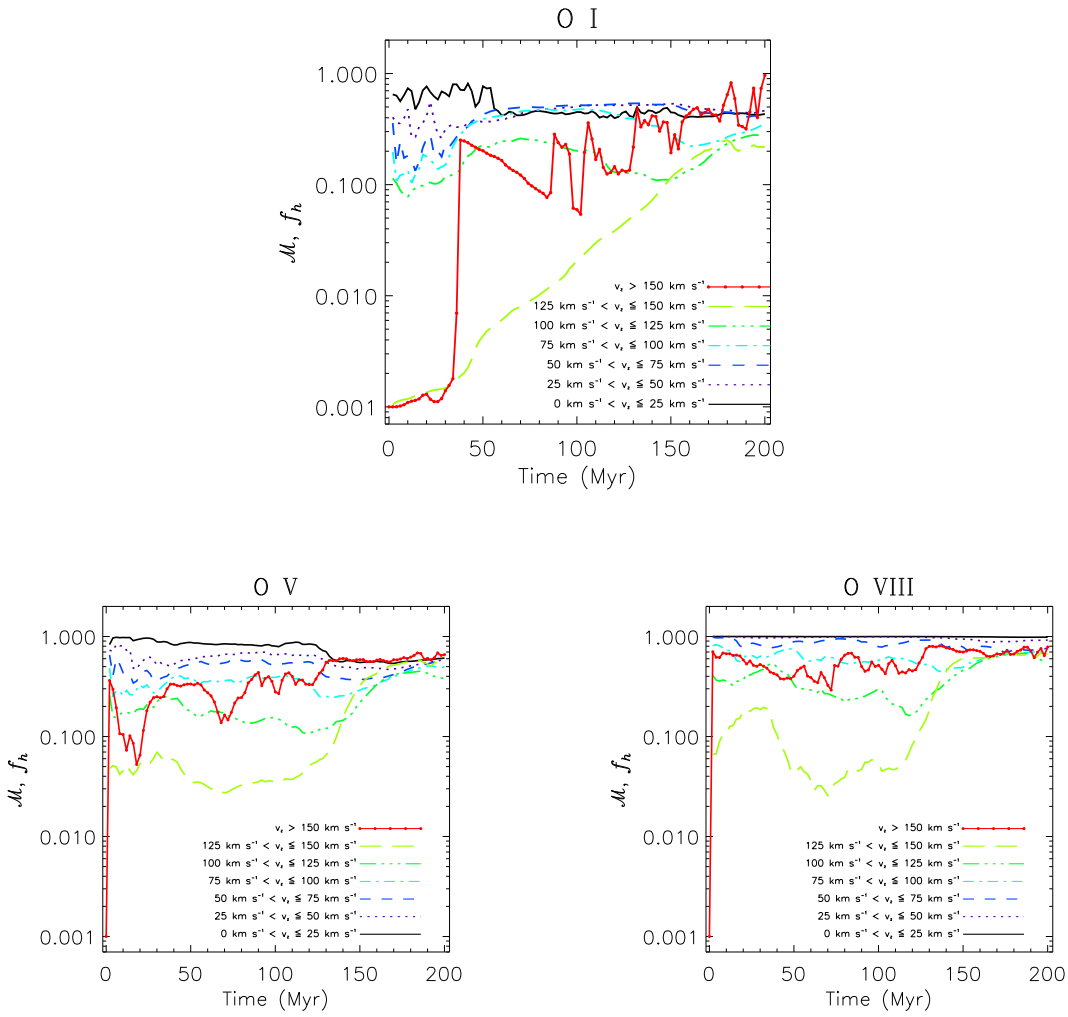

Figure 2.5: Velocity Selections

Average metallicity ($\bar{\mathcal{M}}$) and halo gas fractions (f_h) as functions of time for O I, O V, and O VIII plotted using various velocity selections. For clarity we only show Model B and separate the velocity ranges with differing line styles.

Chapter 3

Condensation Of Halo, Circumgalactic, And Intergalactic Gas Onto Massive High Velocity Clouds[1]

[1]Gritton, Jeffrey A., Shelton, Robin L., and Galyardt, Jason E., 2016. Submitted to *The Astrophysical Journal*, reproduced by permission of the AAS

3.1 Introduction

High velocity clouds (HVCs) are classically defined as gas with speeds that differ from the local standard of rest by at least 90 km s^{-1} (see Wakker & van Woerden 1997). Both neutral and ionized high velocity material has been observed (Hill et al. 2009; Putman et al. 2012; Murphy et al. 1995; Lockman et al. 2002; Shull et al. 2009; Collins et al. 2009; Sembach et al. 2003; Lehner et al. 2012). Proposed origins include feedback (or fountain), accretion of satellite galaxies, and accretion from the intergalactic medium. In the fountain model (e.g., Shapiro & Field 1976; Bregman 1980), gas is propelled to heights of a few kpc above the disk by stellar winds and supernova explosions. The material can later fall back onto the disk. The process of accreting satellite galaxies occurs over a larger length scale. Material can be stripped from nearby satellite galaxies by ram pressure and tidal forces. The Magellanic Stream (see Wakker & van Woerden 1997; Putman et al. 2012) is an example of such stripped material. The stripped material can then fall towards the Galactic disk and, if it does not mix with the ambient environment in the halo (Kwak et al. 2011; Putman et al. 2012; Gritton et al. 2014) to the point of homogeneity, it could accrete onto the disk. Lastly, condensation along intergalactic filaments could yield extragalactic HVCs. This condensation has been shown in simulations (Joung et al. 2012) and seen in observations of H I between M31 and M33 (Wolfe, Lockman, & Pisano 2016).

HVCs of extragalactic origin may be an important mechanism for delivering fresh material to the disk (Twarog 1980; Wakker et al. 1999; Lehner & Howk 2011; Putman et al. 2012; Plöckinger & Hensler 2012) allowing our Galaxy to continue forming stars at a high rate for a longer period of time. The current rate at which gas in the Milky Way is converted into stars is thought to be between $\sim$1 and $\sim$3 $M_{\odot}$ yr^{-1} (see Putman et al. 2012, and references therein). In order to deliver their material to the disk, extragalactic HVCs would have traversed great distances. Furthermore, if HVCs condense material while traversing the halo or intergalactic space, then their likelihood of surviving to reach the disk is increased as would the amount of mass they can provide to the Milky Way.

Smaller clouds, like those generated by fountains, have been simulated elsewhere. Heitsch & Putman (2009) studied relatively small clouds with masses between 1.4×10^3 $M_\odot$ and 44×10^3 $M_\odot$ and found that the clouds tended to disrupt and evaporate over the course of the hydrodynamic simulations. Using different initial parameters and/or cooling rates, Marinacci et al. (2010) performed hydrodynamic simulations of clouds with masses between 4.4×10^3 $M_\odot$ and 4.4×10^4 $M_\odot$ and found that these small clouds can condense between $\sim$1% and $\sim$4% of the initial cloud mass from the ambient environment. Thus, the small clouds that have been simulated thus far either evaporate or only mildly condense.

Fraternali et al. (2015) consider the case of a very massive, solar metallicity, cloud (3.4×10^6 $M_\odot$) near the Galactic plane in the context of a fountain model. In their 2-dimensional hydrodynamical models using solar metallicity cooling rates, the cloud and its wake condense material from the Galaxy's thick disk weighing up to $\sim$100% of the cloud's initial mass. Condensed environmental material could extend the lifetimes of HVCs and supplement the mass that can be delivered to the Galactic disk. This raises the question of how condensation affects massive clouds of extragalactic origins. Can they also condense material as they travel through the Galactic halo and extragalactic space?

In this paper we perform 3D hydrodynamic simulations of clouds with masses ranging from 1.35×10^5 $M_\odot$ to 1.35×10^8 $M_\odot$ making them comparable to objects like Complex WE and the Magellanic Stream (see Wakker 2001), respectively. As they traverse through homogeneous low density gas, like that in the extended halo and intergalactic space, we find that these larger and more massive clouds condense large amounts of material from the ambient environment and that the condensed material continues to retain high ions such as O VI and O VIII even though temperature drops below 1.0×10^4 K. Our methodology and initial parameters are discussed in Section 3.2. In Section 2.3 we present the results of our simulations. Specifically, in Sections 3.3.1 and 3.3.2 we discuss our use of oxygen as a tracer to track material condensed into the clouds, in Section 3.3.3 we discuss general results related to condensation, and in Sections 3.3.3.1, 3.3.3.2, 3.3.3.3, and 3.3.3.4, we discuss the effects of

the initial ambient density, initial cloud density and temperature, initial speed of the cloud, and initial size of the cloud respectively. We summarize and discuss the simulational results in Section 3.4.

3.2 Numerical Code and Initial Parameters

We use FLASH 4.2, see Fryxell et al. (2000) and Dubey et al. (2008), to simulate the hydrodynamic interactions between HVCs and low density surrounding ambient environments. Our simulations model 3-dimensional, fixed, Cartesian domains. We present a series of nine simulations exploring the effects of of densities, speeds, cloud masses, and cloud radii.

We differentiate simulations using a naming convention built from the initial simulation parameters of Table 3.1. The simulations are named by their cloud temperature (T_{cl}), cloud radius (r_{cl}), ambient hydrogen number density (n_{amb}), and cloud speed (v_{cl}). For example, the first simulation in Table 3.1 has T_{cl} = 5,000 K (T5), r_{cl} = 300 pc (r3), $n_{amb} = 10^{-3}$ cm^{-3} (n3), and v_{cl} = 150 km s^{-1} (v150) and is therefore named T5r3n3s150.

Our FLASH simulations modeled the radiative cooling of the gas, however FLASH does not currently simulate metallicity-dependent radiative cooling or use different cooling curves for different cells. To account for the range of metallicities in the domain, we use the Sutherland & Dopita 1993 cooling curve for a plasma with a metallicity of $\mathcal{M}$=$10^{-0.5}$ $\mathcal{M}_{\odot}$.

In order to minimize the computational requirements we also use an adaptively refinable mesh whose cell sizes are allowed to differ from each other and vary during the simulation. However, as part of the post-production analysis the original refined mesh is mapped onto a uniform grid, all of whose cells have equal spatial dimensions equal to the smallest cell in the grid. The maximum resolution of all simulations equates to ∼32 cells per cloud radius. This is of higher resolution than the lower bound of 25 cells per cloud radius suggested by Mac Low & Zahnle (1994). In order to test for convergence we ran simulations with identical physical parameters to T5r3n3s150 with maximum resolutions of ∼16 cells per cloud radius and ∼64 cells per cloud radius. Values for high velocity cool condensed mass do not vary by

more than a fraction of a percent while values of cool mass approach similar values within a few percent of each other. Therefore we are confident that our maximum resolution of ∼32 cells per cloud radius is adequate. For domain sizes and spatial resolutions see Table 3.2.

We assume symmetry across some boundaries to reduce the computational demands. Simulations T5r3n3s150, T5r3n4s150, T5r3n3s300, T20r3n3s300, T10r3n3s300, T4r3n3s300, T5r3n4s300 assume symmetry across the $y = 0$ pc plane so we simulate only $\frac{1}{2}$ of the cloud. Simulations T5r15n4s300 and T5r30n4s300 assume symmetry across both the $x = 0$ pc and $y = 0$ pc boundaries so we simulate only $\frac{1}{4}$ of the cloud. For the purpose of this paper, reported masses will be scaled by factors of 2 or 4 when only $\frac{1}{2}$ or $\frac{1}{4}$, respectively, of the cloud is simulated such that the mass of a whole cloud is reported.

We place our cloud at $x = 0$ pc, $y = 0$ pc, and $z = 0$ pc in all of our models. At the beginning of each simulation, the density of hydrogen in the core of the cloud is nearly uniform, but it decreases rapidly and smoothly from $\sim n_{H,cl}$ to $\sim n_{H,amb}$ following the form

$$n_H(r) = -0.5\,(n_{cl} - n_{amb}) \tanh\left(\frac{r - r_{cl}}{r_{cl}/6}\right) + 0.5\,(n_{cl} + n_{amb})$$

where n_{cl} and n_{amb} are the hydrogen number densities of the cloud material and ambient material respectively, r is the radial distance from the center of the cloud, and r_{cl} is the chosen cloud radius. We impose pressure balance throughout the domain in the initial configuration, which requires the temperature to increase in proportion to $\frac{1}{n_H(r)}$ in the vicinity of r_{cl}. Ambient material is given a temperature of T_{amb}=2×10^6 K, like that in the Galactic halo (Henley & Shelton 2015), for all models. Similar density and temperature distribution functions were used in Heitsch & Putman (2009), Kwak et al. (2011), and Gritton et al. (2014) and are reflective of the cloud edge characteristics observed by Burton et al. (2001). Furthermore, Vieser & Hensler 2007 note that simulated clouds with smooth density transitions are less prone to disruptions than are clouds with sharp boundaries. Unlike the density and temperature, the velocity and metallicity have a step function boundary at a radius that

contains ∼99% of the cloud's mass. The simulations are run within the rest frame of the cloud so that all gas within the cloud is initially given zero velocity in all directions and so that the ambient material is given an initial velocity in the positive z-direction and is allowed to flow into the domain from the lower z-boundary. However, for the purpose of this paper we will report all velocities from the rest frame of the ambient material.

To compare clouds in disparate areas of parameter space, we use compare using three time scales the cloud crushing time (t_{cc}) defined as $t_{cc} = \frac{r_{cl}\ \chi^{1/2}}{v_{cl}}$ by Klein et al. (1994) where r_{cl} is the cloud radius, v_{cl} is the cloud speed, and χ is the density contrast between the cloud and ambient medium $\left(\chi = \frac{n_{cl}}{n_{amb}}\right)$. The cloud crushing time can be interpreted as the time required for a shock to traverse the cloud and can be related to the amount of time for a cloud to evolve to a certain point. The use of cloud crushing time has been implemented in studies like those by Mellema et al. (2002), Fragile et al. (2004), Melioli et al. (2005), Cooper et al. (2009), Marinacci et al. (2010, 2011), Kwak et al. (2011), Scannapieco & Brüggen (2015), and Schneider & Robertson (2017). In addition, in order to disentangle the effects of material leaving the domain from other effects that we are interested in, we define a cloud leaving time (t_L) which is when at least ∼0.2% of the initial cloud mass in cool material ($T \leq$10,000 K) has been swept from the domain. The ambient material can also be described by its cooling time ($t_{cool,amb}$) and the sound speed within the medium (c_s). The cooling time is calculated by $t_{cool,amb} = \frac{3}{2}\frac{k_B\ n_{amb}\ T_{amb}}{n_{amb}^2\ \Lambda}$, where T_{amb} is the ambient temperature ($T_{amb} = 2 \times 10^6$ K), Λ is the cooling coefficient from our choice of cooling curves ($\Lambda(T_{amb}) = 10^{-22.34}$ erg cm^{-3} s^{-1}), k_B is the Boltzmann constant, and n_{amb} is the hydrogen number density of the ambient material. The sound speed in the ambient medium is $c_s = \left[\frac{\gamma\ k_B\ T_{amb}}{\bar{m}}\right]^{\frac{1}{2}}$, where $\bar{m}$ is the average particle mass, and $\gamma = \frac{5}{3}$. All models share the same T_{amb} and $\bar{m} = 0.6$ in units of hydrogen mass so that $c_s = 214$ km s^{-1}. The values described here, as well as the cloud's Mach number $\mathbf{M}_{\#}$, are presented in Table 3.3.

For this paper, we use the solar abundances of Anders & Grevesse 1989; e.g., 9.77×10^{-2}, 3.63×10^{-4}, 1.21×10^{-4}, and 8.51×10^{-4} heliums, carbons, nitrogens, and oxygens per hydro-

gen for the ambient material for the purpose of later tracing the material. Here, like in Gritton et al. (2014), we define metallicity ($\mathcal{M}$) as the ratio of the abundance of a given element to the solar abundance of that element. The real metallicities of clouds and their ambient environment vary and are not always predetermined. For this reason we set the metallicities of our cloud to $\mathcal{M}_{\rm cl}$=0.001 $\mathcal{M}_{\odot}$ and ambient material to $\mathcal{M}_{\rm amb}$=1.0 $\mathcal{M}_{\odot}$ so that the results can be easily scaled, and so that we can easily track the flow of ions from the ambient material into the cloud material.

The ionization levels of these ions are tracked in each cell in a time-dependent manner using FLASH's non-equilibrium ionization (NEI) module. We use the ions of oxygen as tracers of the mixing and condensation of ambient material into our pristine cloud. The metallicity of any given cell in the domain is a result of the contributions from the cloud and the ambient material. The metallicity of a cell is defined as $f_{amb}\mathcal{M}_{\rm amb}+f_{cl}\mathcal{M}_{\rm cl}$, where f_{amb} and f_{cl} are the ratios of the ambient gas mass and cloud gas mass, respectively, to the total mass in the cell.

3.3 Results

3.3.1 Condensation

In order to prove the concept that oxygen can be a tracer of condensation, we show the density along the x-z plane in Simulations T5r3n3s150 and T5r3n3s300 in Figure 3.1, and we choose four cells of cooled gas within the cloud structure, marked in the upper images of Figure 3.1 by circles that are centered on the chosen cells. The lower plots of Figure 3.1 show the abundance of oxygen ($\frac{O}{H}$) present in each of the chosen cells plotted versus the ionization state of oxygen in ascending order of the number of electrons lost. Even in cool cells (T <5,500 K), highly ionized oxygen (i.e., O v, O vi, O vii, O viii, & O ix) is present along with the ions that one would expect (i.e., O i, O ii, O iii, & O iv) at low temperatures assuming only collisional ionization equilibrium. The high metallicity and

presence of highly ionized oxygen at low temperatures indicates that some material from the ambient environment has condensed onto the cloud.

3.3.2 Ionization States of Oxygen as a Tracer of Condensation

We measure the amount of ambient material that is condensing into the HVC structure within the simulated domain as a function of time (Figure 3.2) [2]. Because we want condensed gas, we impose two criteria: that the selected gas be cool (here we require $T \leq$10,000 K) and that it contain material from the ambient environment (here we require $f_{amb} \geq 0.1$, but later in the paper, other thresholds will be examined). Any gas that meets both of these criteria will have experienced substantial radiative cooling from a hot temperature. For example, any cell that meets both of these criteria in Simulation T4r3n3s300, in which T_{amb}=2×10^6 K and T_{cl}=4,000 K, will have cooled from T_{ave}=$f_{amb}T_{amb}$+(1-f_{amb})T_{cl}=203,600 K to less than 10^4 K. Any highly ionized oxygen (O VI, O VII, O VIII, and O IX) in such cells must have cooled (i.e.,condensed) from the ambient gas.

Simulations are run for 200 Myr or 400 Myr of simulated time (see Table 3.2), which is long enough for ablated cloud material to begin to flow off the domain. In order to disentangle the effects of material leaving the domain from other effects that we are interested in, we mark the plots of Figures 3.2 & 3.3 with vertical dotted lines when at least ∼0.2% of the initial cloud mass in cool material ($T \leq$10,000 K) has been swept from the domain. We call this time t_L and although we present trends beyond t_L in Figures 3.2 & 3.3, we only compare simulations using times $t \leq t_L$ in our quantitative analysis (Section 3.3.3). Only in Simulation T5r3n3s150 does any cloud material leave the domain before t_L[3]. The shaded regions of the plots denotes time periods when cool material leaves the domain.

The details of the curves in Figure 3.2 relate to the evolutions of the clouds. Vacillation in the growth of the mass for $t \leq t_L$ result form the competition between condensation

[2]We present the masses after scaling by a factor of 2 or 4 for simulations where $\frac{1}{2}$ or $\frac{1}{4}$ of the domain is simulated respectively, so that the presented numbers represent those of a whole cloud.

[3]In Simulation T5r3n3s150, ∼0.1% of the initial cloud mass in cool material exits the domain between 58 Myr and 92 Myr, the time period that is highlighted by the shaded gray band in Figures 3.2 & 3.3.

and evaporation. Even with evaporation, all clouds accumulate mass monotonically. The development of clumps and fragments causes the up-ticks in the curves, like the up-tick seen in T5r3n4s150 at ∼75 Myr. The simultaneous decrease in the masses of multiple ions of oxygen is usually due to material leaving the domain at a faster rate than the ambient material condenses onto the HVC structure. Even after material begins to leave the domain this loss of mass is more than compensated for by the fresh condensation of ambient material for some time, causing the maxima in our mass curves to occur some time after t_L.

One of the more impressive features of these simulations is the large mass of O VII condensed from the ambient material. Simulations with a cloud radius of r=300 pc obtain between 2.5 $M_\odot$ and 500 $M_\odot$ of O VII via condensation from the ambient environment. Larger clouds can condense even more material from the environment due to their increased surface area in contact with the environment and stability against disruption. Simulations T5r15n4s300 and T5r30n4s300 have initial radii of r=1,500 pc and r=3,000 pc respectively. These simulations obtain maximum values of condensed O VII mass between 225 $M_\odot$ and 400 $M_\odot$. Of course, O VII is not the only ionization state of condensed ambient oxygen and oxygen is not the only element that the ambient material is comprised of. Hydrogen and helium will condense with oxygen into the cloud material and be the two greatest contributors to the increase of mass.

3.3.3 Total Condensation

In the previous section we discussed the condensation of only highly ionized oxygen into a HVC. Oxygen is, however, just one of the components of the ambient material. The greatest contributors to mass via condensation will be the hydrogen and helium within the condensing ambient material. Figure 3.3 shows the total scaled mass of cool ($T \leq$10,000 K) gas that has condensed from the ambient material, with various other selection criteria. Solid lines show the mass of cool material in the domain. Dashed lines show the mass of low temperature and high velocity material. These criteria select only cool material moving at speeds in excess

of 100 km s^{-1} in the z-direction in order to focus on material that would be considered a HVC. Different colors show the mass after five f_{amb} selection criteria have been applied to cases with and without the velocity criterion. We only select gas with f_{amb} greater than or equal to a set of minimum values; e.g., $f_{amb}\geq0.1$, $f_{amb}\geq0.2$, $f_{amb}\geq0.3$, $f_{amb}\geq0.4$, $f_{amb}\geq0.5$. This allows us to probe the origins of the mixed material and its location within the cloud structure.

The amount of condensed material varies depending upon the initial parameters of the simulations, but in all cases rises over time until the loss due to material flowing off the domain outpaces condensation. When normalizing the condensed material mass from Figure 3.3 to the initial cloud mass ($\bar{M}=\frac{M_{cond}}{M_{cl}}$, where M_{cond} is the mass of condensed material and M_{cl} is the initial cloud mass), we find that the mass of condensed material can be up to 100% of the initial cloud mass. The amount of condensation ranges from a few percent of the initial cloud mass within the first 50 Myr to ∼100% of the initial cloud mass at ∼200 Myr in our most extreme case. We see condensation throughout the range of f_{amb}, from mixed gas that contains a large concentration of ambient gas (e.g., $f_{amb}\geq50\%$) to gas that contains a small fraction of ambient gas (e.g., $f_{amb}\geq10\%$). In order to compare simulations that have evolved for equal amounts of time under different circumstances without the added complication of material leaving the domain, we select a common time, t=74 Myr, the smallest value of t_L in any simulation. In Figure 3.4 we compare $\bar{M}$ of all simulations at $t = 74$ Myrs using circles. We find all simulations having n_{amb}=10^{-3} cm^{-3} have normalized condensed masses exceeding 10%, while all those having n_{amb}=10^{-4} cm^{-3} have $\bar{M}$ less than 5%. From this we can see that denser ambient environments yield more condensed mass by the chosen time. See Subsection 3.3.3.1. The highest density, lowest temperature clouds condense the greatest amounts of ambient material, but their normalized condensed masses are smaller than those of the clouds that begin with lower densities, higher temperatures. This is described further in Subsection 3.3.3.2. In the subsonic cases more than half of the condensed material slows to intermediate velocities during the simulations, while in the supersonic cases,

almost all of the condensed material remains at high velocities throughout the simulations. This is discussed in greater detail in Subsection 3.3.3.3. We examine two extremely large clouds (r_{cl}=1,500 pc, M_{cl}=1.69×10^7 $M_\odot$, and r_{cl}=3,000 pc, M_{cl}=1.35×10^8 $M_\odot$), finding that as radius increases, the total amount of condensed matter increases, however, the normalized amount of condensed matter ($\bar{M}$) decreases with radius. See Subsection 3.3.3.4. Our largest cloud has a mass of M_{cl}=1.35×10$^8 M_\odot$. Within the 400 Myr of the simulation it only evolves to the beginning stages seen in the other simulations. Thus such clouds can travel much further distances without disruption than can the smaller clouds. This is discussed in Subsection 3.3.3.4.

In Figure 3.4 we show values of $\frac{M_{cond}}{M_{cl}}$ of cool gas (T $\leq$10,000 K) with $f_{amb}\geq$0.1 as a function of time in units of cloud crushing time (t_{cc}) for all simulations. At $\frac{t}{t_{cc}} \leq 2$ all simulations have similar values with the exception of T5r3n3s150which diverges from the other simulations much earlier. The early agreement in values for all but T5r3n3s150 indicates that early condensation onto the clouds is similar despite disparate simulational parameters. However, after $\frac{t}{t_{cc}} \simeq 2.5$ values of $\frac{M_{cond}}{M_{cl}}$ diverge. Circles plotted on each line denotes t_L for each simulations. It can be seen that large amounts of condensation are missed if simulations are only compared at $\frac{t}{t_{cc}} = 2$. Therefore for the remainder of this paper we shall compare simulations using the smaller value of $\frac{t_L}{t_{cc}}$ so that all simulations being compared have the longest possible time to evolve before material begins leaving the domain.

3.3.3.1 Initial Densities

Here we compare simulations in which n_{amb}=10^{-3} cm^{-3} with those that have n_{amb}=10^{-4} cm^{-3} in order to determine if the density affects the condensation of ambient material. We examine two sets of simulations, one in which the cloud speeds are subsonic (v_{cl}=150 km s^{-1}), i.e., Simulations T5r3n3s150 and T5r3n4s150, and one set in which they are supersonic (v_{cl}=300 km s^{-1}), i.e., Simulations T5r3n3s300 and T5r3n4s300. For reference the speed of

sound in the ambient medium is 214 km s^{-1}. We examine the subsonic set at $\frac{t}{t_{cc}}$=3.50, the smaller of the $\frac{t_L}{t_{cc}}$'s for this set and we examine the supersonic set at $\frac{t}{t_{cc}}$=3.85, the smaller of the $\frac{t_L}{t_{cc}}$'s for this set. In both sets, the simulations with the greater densities condense more mass than their less dense counterparts and yield greater normalized condensed masses, $\bar{M}$. In the subsonic set, Simulation T5r3n3s150 has condensed 30.3 times more mass than Simulation T5r3n4s150 has and its normalized condensed mass is 3.03 times larger than that of Simulation T5r3n4s150 at $\frac{t}{t_{cc}}$=3.50. In the supersonic set, Simulation T5r3n3s300 has condensed 40.9 times more mass than Simulation T5r3n4s300 and its normalized condensed mass is 4.09 times larger than that of T5r3n4s300 at $\frac{t}{t_{cc}}$=3.85. The reason why the denser member of each set is the more effective condenser of ambient material within the chosen timespans is because the cooling rate per specific heat is proportional to density.

In the upper two panels of Figure 3.3, the difference between the total mass of condensed gas (shown by the solid lines) and the mass of high velocity condensed gas (shown by the dashed lines) is the mass of slow and intermediate velocity condensed mass and is growing rapidly with time. Condensation occurs in both the head and the tail of each cloud and in both the fastest and slowest cloud material, however the decelerated material in the tail is especially rich in condensed gas. The slow and intermediate velocity condensed mass is not as prevalent in the supersonic cases as in the subsonic cases because the material would have to decelerate much more in order to fall below the velocity threshold for HVC gas.

3.3.3.2 Initial Cloud Density and Temperature

In order to explore the effects of initial cloud density and temperature, we run a series of simulations, all of which have the same cloud speed (v_{cl}=300 km s^{-1}), cloud radius (r_{cl}=300 pc), ambient density (n_{amb}=10^{-3} cm^{-3}), and ambient temperature (T_{amb}=2×10^6 K), but each of which has a different cloud density and, by application of pressure balance, a different cloud temperature. These simulations are T20r3n3s300, T10r3n3s300, T5r3n3s300, and T4r3n3s300 whose (n_{cl}, T_{cl}) are (0.1 cm^{-3}, 2×10^4 K), (0.2 cm^{-3}, 1×10^4 K), (0.4 cm^{-3},

5×10^3 K), and (0.5 cm^{-3}, 4×10^3 K) respectively. As simulational time progresses, the denser cooler clouds develop wider tails with a larger number of trailing clumps than do the less dense clouds. The simulations with denser cooler initial clouds result in more condensed mass. For example, at $\frac{t}{t_{cc}}$ for this set of simulations ($\frac{t_L}{t_{cc}}$=3.50 from Simulation T10r3n3s300), the condensed masses (M_{cond}) are, in order of increasing initial cloud density: $M_{cond,\ T20r3n3s300}$=19,800 $M_\odot$, $M_{cond,\ T10r3n3s300}$=60,100 $M_\odot$, $M_{cond,\ T5r3n3s300}$=183,000 $M_\odot$, and $M_{cond,\ T4r3n3s300}$=259,000 $M_\odot$. This may be due to the greater amount of material in the tails of denser and cooler clouds providing more sites for condensation to occur. It could also be due to the greater density gradient between cloud and ambient gas, which Vieser & Hensler 2007 found to lead to more ablation and fragmentation. For both of these reasons, denser cooler clouds yield tails of ablated cool material that have greater volumes and surface areas in contact with the bath of ambient material, resulting in more condensation of ambient gas. Furthermore, the mixed gas behind initially cooler clouds begins with a temperature that is nearer to our temperature selection criterion and can therefore radiatively cool to our temperature selection criterion in a shorter amount of time.

3.3.3.3 Initial Speed

Here we analyze the effects of initial speed on condensation. We compare two sets of simulations. Each set contains one subsonic and one supersonic simulation. The first set of simulations, referred to as the high density set, contains subsonic simulation T5r3n3s150 and supersonic simulation T5r3n3s300 where both simulations have clouds that have an initial hydrogen number density of n_{cl}=0.4 cm^{-3}, initial temperature T_{cl}=5,000 K, and initial cloud radius r_{cl}=300 pc and are in an ambient environment with n_{amb}=10^{-3} cm^{-3} and ambient temperature T_{amb}=2×10^6 K. The second set of simulations, referred to as the low density set, contains subsonic simulation T5r3n4s150 and supersonic simulation T5r3n4s300 where both simulations have clouds that have an initial hydrogen number density of n_{cl}=0.04 cm^{-3}, initial temperature T_{cl}=5,000 K, and initial radius r_{cl}=300 pc and are in an ambient en-

vironment with n_{amb}=10^{-4} cm^{-3} and ambient temperature T_{amb}=2×10^6 K. Instabilities disrupt the subsonic clouds in both sets, although the resulting structures differ. Simulation T5r3n3s150 becomes well mixed but does not fragment while Simulation T5r3n4s150 becomes highly fragmented. In contrast, in the supersonic simulations the high sheer speeds damp some instabilities allowing the HVCs to form smooth head-tail structures. We examine each simulation at the smallest $\frac{t_L}{t_{cc}}$ in its set (e.g., we examine both Simulations T5r3n3s150 and T5r3n3s300 at $\frac{t}{t_{cc}}$=3.85 and T5r3n4s150 and T5r3n4s300 at $\frac{t}{t_{cc}}$=3.50). The high density HVCs T5r3n3s150 and T5r3n3s300 condense $M_{cond,\ T5r3n3s150}$=984,000 $M_\odot$ and $M_{cond,\ T5r3n3s300}$=233,000 $M_\odot$ at $\frac{t}{t_{cc}}$=3.85. The low density HVCs T5r3n4s150 and T5r3n4s300 condense $M_{cond,\ T5r3n4s150}$=27,200 $M_\odot$ and $M_{cond,\ T5r3n4s300}$=3,960 $M_\odot$ at $\frac{t}{t_{cc}}$=3.50. The greater mass condensed onto the subsonic clouds at these comparable $\frac{t}{t_{cc}}$ shows the importance of instabilities as a mechanism to capture condensing material into a HVC as instabilities are damped in the supersonic clouds. Of course the masses condensed onto the denser HVCs greatly outweighs those condensed onto the less dense HVCs, making cloud and ambient density more important than velocity.

3.3.3.4 Initial Cloud Radius

We compare the effects that the initial cloud radius has on the condensation of ambient material. Simulations T5r3n4s300, T5r15n4s300, and T5r30n4s300 are all supersonic simulations with n_{cl}=0.04 cm^{-3} and n_{amb}=10^{-4} cm^{-3}. However, the initial radii of the clouds differ and are 300 pc, 1,500 pc, and 3,000 pc for Simulations T5r3n4s300, T5r15n4s300, and T5r30n4s300 respectively. As the clouds become larger, instabilities are damped causing larger clouds to be more supported against destabilization. As the cloud radius increases so does the amount of condensed material. Using $\frac{t_L}{t_{cc}}$=2 from Simulation T5r30n4s300 we find that the clouds condense masses of $M_{cond,\ T5r3n4s300}$=189 $M_\odot$, $M_{cond,\ T5r15n4s300}$=455,000 $M_\odot$, and $M_{cond,\ T5r30n4s300}$=5,470,000 $M_\odot$. Similarly, the amount of material condensed normalized to the initial mass of the cloud increases with increasing radius; $\bar{M}_{T5r3n4s300}$=0.0011,

$\bar{M}_{T5r15n4s300}$=0.022, $\bar{M}_{T5r30n4s300}$=0.033. This is likely due to the larger clouds having larger surface areas so they can condense ambient material more effectively than smaller clouds.

3.4 Summary and Discussion

We simulated a suite of massive HVCs using the FLASH hydrodynamic code in order to examine the exchange of material between the clouds and their environments. Over long periods of time our simulated HVCs condense more halo material than they lose to evaporation. Here, we define condensed ambient gas as material that has cooled from its initial temperature (2×10^6 K) to less than 1×10^4 K after mixing with cloud material. The masses of condensed material range from 3×10^4 $M_\odot$ on a cloud with an initial mass of 1.35×10^5 $M_\odot$, which is comparable in mass to the AC Shell or Complex WE (see Wakker 2001), to 6×10^6 $M_\odot$ on a cloud with an initial mass of 1.35×10^8 $M_\odot$, which is on the order of the Magellanic Stream (see Wakker 2001). The ratio of condensed mass to the initial cloud mass ranges from 0.16% to 100% with larger clouds condensing more mass, but being proportionally less effective than smaller clouds.

We tested the effects on condensation of the initial density, radius, temperature, and speed of the cloud and the initial density of the ambient gas. Denser ambient gas condenses more easily onto clouds. Similarly, denser, cooler clouds are more efficient at condensing material because they are easily fragmented, creating a clumpy tail where substantial condensation occurs. Supersonic clouds are somewhat protected by their bow shocks. Also their high speeds suppress instabilities. They experience sheer which pulls their material into long tails where substantial condensation occurs. However, they do not condense as much material as their subsonic counterparts, showing that the damping of instabilities due to supersonic speeds reduces the the amount of condensed material. Clouds with larger radii condense more ambient material due to their larger surface areas.

Our finding that smaller, less massive clouds and shorter timescales yielded far less efficient condensation is consistent with the work of Heitsch & Putman 2009 and Marinacci

et al. (2010). All of the clouds simulated by Heitsch & Putman 2009 and Marinacci et al. (2010) were smaller and less massive than ours. Although it is not possible to make direct comparisons between their runs and ours because of differences in physical parameters (e.g. metallicity, speed, and ambient density), criteria used to determine cooled mass, and simulation duration, their clouds tended to evaporate or mildly condense, while ours tended to substantially condense. Likewise, our finding that higher ambient densities (and therefore pressures) led to more condensation, based on simulations of clouds of mass 1.35×10^5 $M_\odot$ to 1.35×10^8 $M_\odot$, follows the same trend as that of Marinacci et al. (2010) who examined smaller less massive clouds than we have ($\sim10^4$ $M_\odot$).

Based on 2-dimensional simulations of a solar metallicity cloud plus calculations of fountain particle trajectories, Fraternali et al. (2015) concluded that fountain gas can condense gas from the thick disk and halo. Their fountain and condensation scenario provides a mechanism for cooling halo gas and transporting it to the Galactic disk. Similarly, our 3-dimensional simulations of 1.35×10^5 $M_\odot$ to 1.35×10^8 $M_\odot$ mass clouds with a subsolar cooling rate also showed significant condensation of ambient gas. Within our suite of simulations, Simulation T5r3n3s150 is most similar to that of Fraternali et al. (2015), although our cloud evolves in a somewhat more rarefied (10^{-3} cm^{-3}) ambient medium than theirs. This simulation condensed ambient material equal to 80% of the clouds initial mass within 160 Myr and more afterwards. Our suite of simulations modeled clouds in ambient media whose density ranged from 10^{-3} cm^{-3} to 10^{-4} cm^{-3}, like that in the halo, circumgalactic, and intergalactic environments. These clouds condense ambient material, indicating that clouds of extragalactic origins can also accrete significant amounts of halo and circumgalactic gas and depending, upon the cloud's trajectories, deliver it to the disk of the Milky Way.

In conclusion HVCs, whether originating in our Galaxy or externally, can accrete considerable amounts of halo and/or circumgalactic gas. This will affect their metallicities and play a role in bringing low metallicity halo and circumgalactic material into the disk when such clouds reach the disk. In addition, condensation will extend their lifetimes and the

Table 3.1. Simulation Initial Parameters

Model	n_{cl} (cm^{-3})	T_{cl} (K)	r_{cl} (pc)	n_{amb} (cm^{-3})	M_{cl} ($r \leq r_{cl}$) ($\times 10^5$ $M_\odot$)	M'_{cl} ($v_i = v_{cl}$) ($\times 10^5$ $M_\odot$)	v_{cl} ($\hat{z}$) (km s^{-1})
T5r3n3s150	0.4	5,000	300	0.001	13.5	16.7	-150
T5r3n4s150	0.04	"	"	0.0001	1.35	1.67	"
T5r3n3s300	0.4	"	"	0.001	13.5	16.7	-300
T20r3n3s300	0.1	20,000	"	"	3.39	4.22	"
T10r3n3s300	0.2	10,000	"	"	6.77	8.38	"
T4r3n3s300	0.5	4,000	"	"	16.9	20.9	"
T5r3n4s300	0.04	"	"	0.0001	1.35	1.67	"
T5r15n4s300	"	"	1,500	"	169	209	"
T5r30n4s300	"	"	3,000	"	1,350	1,670	"

Note. — Initial physical parameters for all simulations. All simulations begin with an ambient material temperature T_{amb}=2×10^6 K. Columns from left to right are; initial cloud hydrogen number density, initial cloud temperature, initial cloud radius, initial ambient hydrogen number density, initial scaled mass contained within the defined cloud radius, initial scaled mass defined with the initial cloud velocity in the rest frame of the ambient material, initial cloud velocity in the $\hat{z}$ direction and in the rest frame of the ambient material. Masses are scaled by a factor of 2 or 4 when only $\frac{1}{2}$ or $\frac{1}{4}$ of the cloud is simulated.

distances they can travel. Thus condensation has the potential to allow massive clouds of extragalactic origins to traverse the great distances needed to reach the disk of the Galaxy.

Table 3.2. Model Domains

Model	Domain Limits			Fraction of cloud	Min Ref	Max Ref	Simulated Time (Myr)
	x (kpc)	y (kpc)	z (kpc)		x,y,z (pc)	x,y,z (pc)	
T5r3n3s150	$-1.2 \leq x \leq 1.2$	$0 \leq y \leq 1.2$	$-1.2 \leq z \leq 9.6$	$\frac{1}{2}$	38	9	200
T5r3n4s150	"	"	"	"	"	"	"
T5r3n3s300	"	"	"	"	"	"	"
T20r3n3s300	"	"	"	"	"	"	"
T10r3n3s300	"	"	"	"	"	"	"
T4r3n3s300	"	"	"	"	"	"	"
T5r3n4s300	"	"	"	"	"	"	"
T5r15n4s300	$0 \leq x \leq 6.0$	$0 \leq y \leq 6.0$	$-6.0 \leq z \leq 24.0$	$\frac{1}{4}$	188	47	400
T5r30n4s300	$0 \leq x \leq 12.0$	$0 \leq y \leq 12.0$	$-12.0 \leq z \leq 24.0$	$\frac{1}{4}$	375	94	400

Note. — Initial domain parameters for each simulations. Columns from left to right are; domain limits in the x, y, and z directions, fraction of the cloud simulated within the domain, minimum spatial refinement cell size, maximum spatial refinement cell size, and simulated time duration.

Table 3.3. Calculated Simulation Parameters

Model	χ	t_{cc} (Myr)	t_L (Myr)	$t_{cool,amb}$ (Myr)	$\mathbf{M}_{\#}$
T5r3n3s150	400	40	163	287.3	0.7
T5r3n4s150	"	40	140	2,873	"
T5r3n3s300	"	20	77	287.3	1.4
T20r3n3s300	100	10	86	"	"
T10r3n3s300	200	14	74	"	"
T4r3n3s300	500	22	78	"	"
T5r3n4s300	400	20	121	2,873	"
T5r15n4s300	"	100	340	"	"
T5r30n4s300	"	200	400	"	"

Note. — Calculated simulation parameters. From left to right these are the density contrast between the central cloud material hydrogen number density and ambient material hydrogen number density, the cloud crushing time, the visually determined leaving time, the cooling time for the ambient material, and the Mach number for the cloud in the ambient medium where the sound speed of the ambient material, having an average particle mass of $\bar{m} = 0.6$, is $c_s = 214$ km s^{-1}.

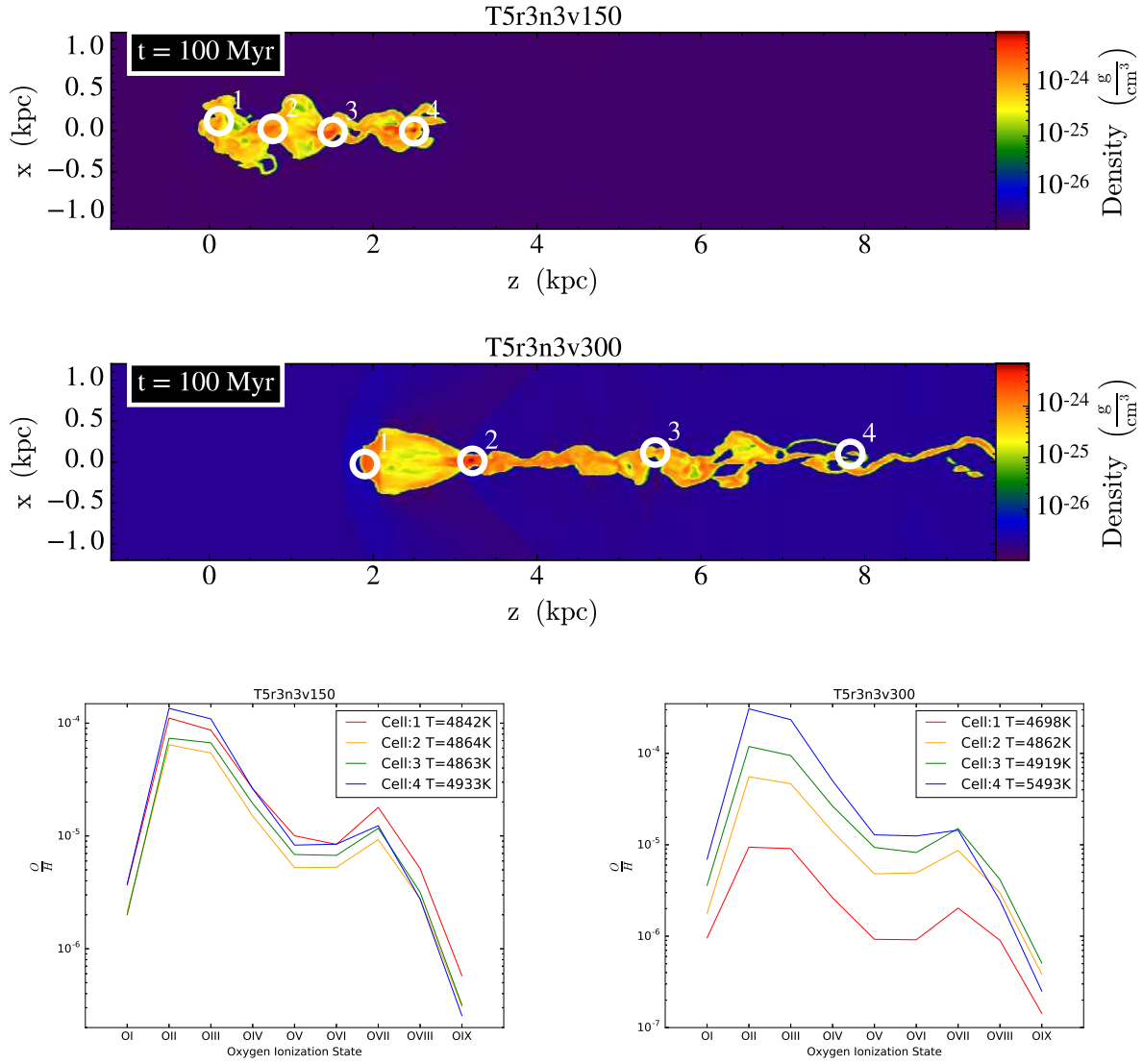

Figure 3.1: Example Sightlines

The top panels depict the density along the x-z plane in the domains of Simulations T5r3n3s150 & T5r3n3s300. The circles are centered on four cells that were chosen from dense clumps within the head-tail structure. From these cells the abundances of oxygen ($\frac{O}{H}$) in each ionization state of oxygen are extracted and plotted as the abundance versus the ionization state of oxygen in the lower two panels. In each cell there exists some highly ionized material mixed with cooler marginally ionized material at low temperatures (T >5,500 K). The highly ionized oxygen at low temperatures indicates that some ambient material has condensed into the cloud.

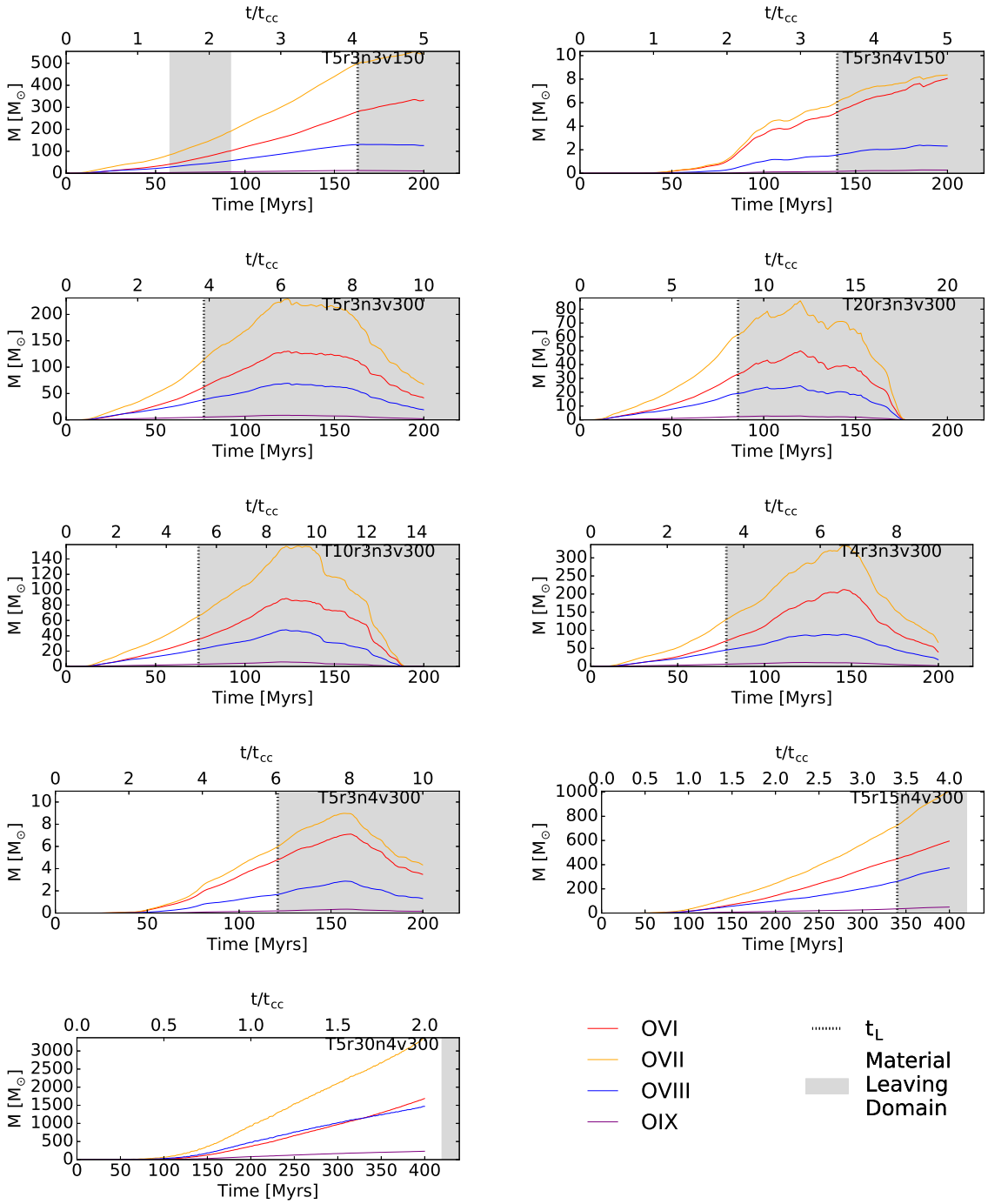

Figure 3.2: Oxygen Condensation

Plots showing highly ionized oxygen with temperatures T $\leq$ 10,000 K. Vertical lines mark the times when material leaves the domain. The vertical dotted line marks the time chosen as t_L, and shaded areas indicate when cool material leaves the domain. All graphs have a single shaded area with the exception of Simulation T5r3n3s150. In this case a small amount of material separates from the cloud body and is swept quickly from the domain. This small mass is only $\sim$0.1% of the cloud mass and once it has left the domain the simulation has no more cloud material flowing off the domain until the vertical dotted line and shaded area at a time of 165 Myr. Note: Masses reported have been corrected for the assumptions of symmetry used in our simulations so that the above masses are as if a full cloud has been modeled.

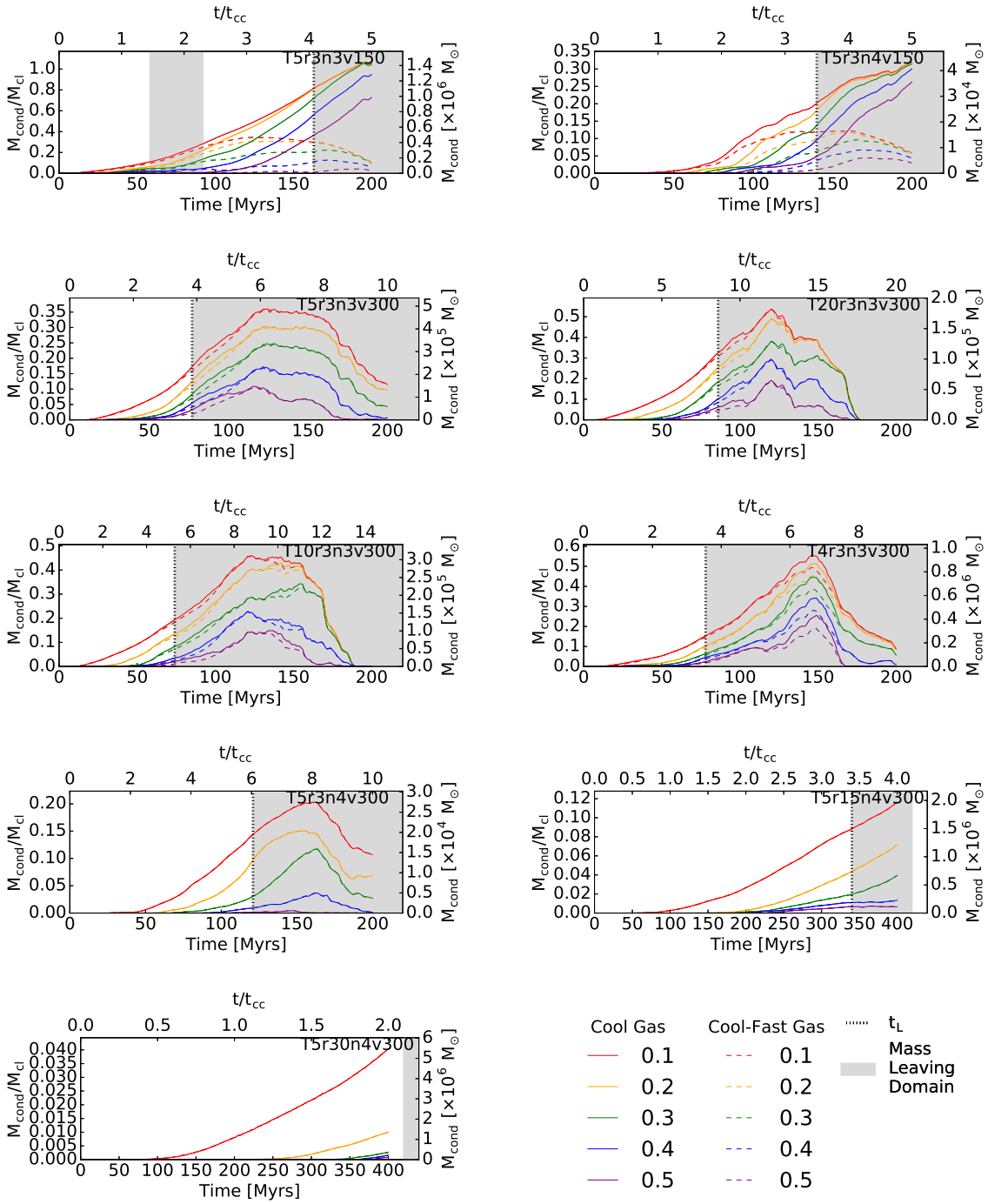

Figure 3.3: Total Condensation

Mass of cooled ($T \leq$10,000 K) mixed gas. The mass of gas whose composition is at least $f_h \geq 0.1$ ambient gas is plotted in red, while yellow, green, blue, and purple signify composition thresholds of 0.2, 0.3, 0.4 and 0.5 respectively. The solid colored curves indicate no velocity threshold, while the dashed colored curves indicate the mass of cooled mixed gas that moves at $v_z \geq 100$ km s^{-1} in the reference frame of the ambient material. The vertical dotted line marks the time we define as t_L. Shaded regions mark times when cloud material is swept off of the domain by the flow of gas around it. Reported masses have been scaled by factors of 2 or 4 when only $\frac{1}{2}$ or $\frac{1}{4}$, respectively, of the region is simulated, so as to account for the entire cloud.

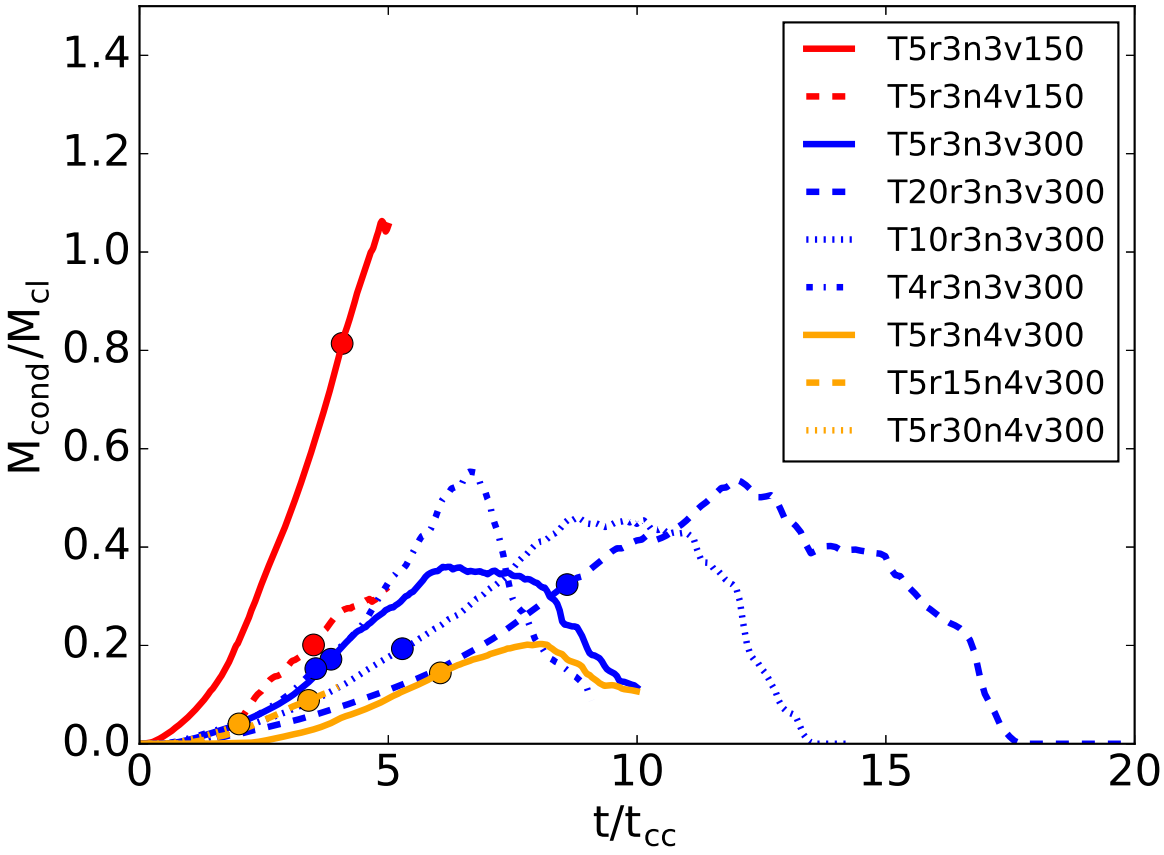

Figure 3.4: global Comparison

A global comparison of the normalized condensed mass ($\frac{M_{cond}}{M_{cl}}$) as functions of time in units of cloud crushing times (t_{cc}) for all simulations. Circles indicate a simulation's t_L value.

Chapter 4

The Evolution Of Massive Magnetohydrodynamic High Velocity Clouds In Uniform Magnetic Fields[1]

[1]Gritton, Jeffrey A., Shelton, Robin L., and Galyardt, Jason E., 2017, To be submitted to *The Astrophysical Journal Letters*.

4.1 Introduction

High velocity clouds (HVCs) are clouds of neutral and ionized gas in the Galactic halo whose motions are not explained by Galactic rotation (see Wakker & van Woerden 1997). As these cool clouds move through the hot ambient medium of the Galactic halo or the intergalactic medium (IGM) they interact with the ambient material. This interaction is drive by sheer flows resulting in instabilities at the interface between the cloud and the ambient material (Kwak & Shelton 2010). The instabilities that form cause a number of processes like ablation of cloud material, fragmentation of the cloud, metal enrichment or dilution of the cloud material (Gritton et al. 2014), and condensation of ambient material onto the cloud or evaporation of cloud material (Gritton et al. 2017).

It has been shown that the inclusion of magnetic fields can damp Kelvin-Helmholtz instabilities between sheer flow layers of fluids (Chandrasekhar 1961; Miura 1984; Malagoli et al. 1996) and effect the motions of astrophysical fluids (Santillán et al. 1999; Raley et al. 2007; Kwak et al. 2009; Galyardt & Shelton 2016).

Kwak et al. (2009) used 3-dimensional magnetohydrodynamic (MHD) simulations to determine the effects of a magnetic fields on HVCs created in a fountain model (e.g., Shapiro & Field 1976; Bregman 1980). Fountain model clouds are ejected from the Galactic disk by stellar feedback. HVCs that originate from being ram pressure and tidally stripped from satellite galaxies, like the Magellanic Stream (see Wakker & van Woerden 1997; Putman et al. 2012), or condensed from the IGM (Joung et al. 2012; Wolfe et al. 2016) are more massive than their fountain model counterparts. This study poses the question, "How do uniform magnetic fields effect massive clouds in the outer regions of the Galactic halo?"

In the following sections we present our numerical methods, choice of environments, and simulational parameter is Section 4.2. In Section 4.3 we present the results of our simulations. Lastly, in Section 4.4 we summarize the results of our simulations and discuss the results of our work in comparison with other works.

4.2 Numerical Code and Initial Parameters

We use FLASH 4.2 (see Fryxell et al. 2000; Dubey et al. 2008) to simulate the hydrodynamic and magnetohydrodynamic interactions between HVCs and the ambient environment. We produce five 3-dimensional, fixed, Cartesian domain simulations with varying parameters. HD simulations assume symmetry across the $y = 0$ pc plane to reduce computational demands by only simulating $\frac{1}{2}$ of a cloud. For the purpose of this paper masses and volumes for the HD simulations are scaled by a factor of 2 to report values as though a whole cloud was simulated. HD simulations also use an adaptively refined mesh whose cell sizes are allowed to vary between a minimum spacial resolution of ∼38 pc in the $\hat{x}$, $\hat{y}$, and $\hat{z}$ directions, and a maximum spacial resolution of ∼9 pc in the x, y, and z directions. MHD simulations, however, simulate a full cloud at a constant spacial resolution of of ∼9 pc in the $\hat{x}$, $\hat{y}$, and $\hat{z}$ directions.

We simulate the radiative cooling of the gas by implementing the cooling curves of Sutherland & Dopita (1993). Observational measurements of HVC metallicity commonly finds average values of ∼30% solar metallicity (see). Therefore we choose a cooling curve for a gas with metallicity equal to ∼30% the solar value.

Simulations share a number of parameters in common, see Table 4.1. Clouds with an initial radius of $r_{cl} = 300$ pc are placed at a location of $x = 0$ pc, $y = 0$ pc, $z = 0$ pc within the domain. Cool clouds with a temperature of T_{cl} =5,000 K begin in pressure equilibrium with the hot ambient material with a temperature of $T_{cl} = 2 \times 10^6$ K. Simulations are run in the rest frame of the initial cloud with the ambient material flowing into the domain along the $\hat{z}$ direction with a speed of 150 km s^{-1}. Though simulations are performed in the rest frame of the cloud, speeds reported here will be presented in the rest frame of the ambient material.

We choose a uniform ambient medium with hydrogen number densities of $n_{amb} = 10^{-3}$ cm^{-3} and $n_{amb} = 10^{-4}$ cm^{-3} which is reasonable for clouds at heights greater than 10 kpc above the disk (see Ferrière 1998). Cool clouds (T_{cl} =5,000 K) begin in pressure equilibrium with

the hot ($T_{amb} = 2 \times 10^6$ K) ambient material. This produces clouds with central densities of $n_{cl} = 0.4$ cm^{-3} and $n_{cl} = 0.04$ cm^{-3} for simulations with $n_{amb} = 10^{-3}$ cm^{-3} and $n_{amb} = 10^{-4}$ cm^{-3} respectively. Density transitions from the n_{cl} value to the n_{amb} value radially from the cloud's center following the function:

$$n_H(r) = -0.5\,(n_{cl} - n_{amb}) \tanh\left(\frac{r - r_{cl}}{r_{cl}/6}\right) + 0.5\,(n_{cl} + n_{amb})$$

where n_H is the hydrogen number density as a function of radius (r) and r_{cl} is the cloud radius. In MHD simulations we include a uniform magnetic field that is either perpendicular ($\hat{x}$-direction) or parallel ($\hat{z}$-direction) to the cloud's motion. The magnetic field strength is adopted from Ferrière (1998) using the same height above the plane as our choices for the ambient densities. This results in a field strength of 1 μG.

The simulations can be separated by being purely hydrodynamic or magnetohydrodynamic. The names of the former simulation type begin with "HD" and the latter simulation type begin with "MHD". Simulations are further differentiated by the ambient density. High density simulations with an ambient hydrogen number density of $n_{amb} = 10^{-3}$ cm^{-3} have names containing "n3" while low density cases with an ambient hydrogen number density of $n_{amb} = 10^{-4}$ cm^{-3} have names containing "n4". MHD simulations include a uniform magnetic field with a strength of 1 μG, but with different orientations. In the names of the MHD simulations we also note the direction of the magnetic field. All simulations have clouds moving in the $-\hat{z}$ direction. When the magnetic field points perpendicularly to the cloud motion, i.e. in the $\hat{x}$ direction, we include "$\perp$" in the simulation's name. When the magnetic field points parallel to the cloud's motion, i.e. in the $\hat{z}$ direction, we include "$\parallel$" in the simulation's name. The names and varying initial simulation parameters can be seen in Table 4.2.

4.3 Results

4.3.1 General Behavior

Here we compare the general evolution of the HD clouds and MHD clouds. Simulations that are purely HD show large scale instabilities and undergo large morphological changes. Simulation HDn3 elongates into a large amorphous shape shown in the first panel of Figure 4.1. The cloud's densest leading core follows behind a lower density leading edge. This makes defining a classical head-tail structure difficult. Simulation HDn4 flattens in the $\hat{z}$ direction and fragments into a large number of trailing fragments. Similar to HDn3 this makes it difficult to define a head-tail structure but in that the tail is a composition of many fragments and not a continuous structure.

MHD simulations show an initial compression of the cloud and are drawn out into long head-tail structures. Simulation MHDn3$\perp$ forms a long thing tail and compact head. The gas is decelerated by the combined ram pressure and magnetic pressure. Simulation MHDn4$\perp$ experiences similar effect but the low density of the cloud allows the magnetic pressure to compress the cloud to a very small volume. The clouds low mass does not have sufficient momentum and is quickly decelerated and swept from the domain by ram pressure and magnetic pressure. Simulation MHDn3$\parallel$ develops a much thicker tail than MHDn3$\perp$ and MHDn4$\perp$ and has a larger head than the other members of the MHD set. We can attribute the classic head-tail structure and stable head to a relatively laminar flow around the cloud head as seen in Figure 4.1. Due to this flow around the cloud the cloud is supported against instabilities which in the HD set result in large scale fragmentation and mixing.

4.3.2 Direct Comparisons Between Simulations

Using the plots of Figure 4.2 we compare simulations directly. We analyze the mass weighted average velocity in the $\hat{z}$ direction ($\vec{V}_{bulk,z}$) of cool ($T \leq 10,000$ K) material in the last panel of Figure 4.2. When the cloud's trajectory is perpendicular to the magnetic field

the deceleration of the cloud is large in comparison to simulations lacking a magnetic field. However, when the trajectory is parallel to the magnetic field the cloud is supported against disruptive instabilities and is not affected by the magnetic pressure in the direction of travel. This allows for a smaller drag force from the ram pressure so the cloud is long lived and experiences less deceleration than both the HD set and other MHD simulations.

If we consider the mass of cool ($T \leq 10,000$ K) gas we see differences between HD simulations in the first plot of Figure 4.2. HD simulations experience large numbers of instabilities. For HDn3 this causes high amounts of condensation. Conversely, for Simulation HDn4 the instabilities cause the cloud to fragment and the resulting fragments quickly evaporate in the hot ambient medium. MHD simulations experience a more laminar flow around the cloud head. This supports the cloud head from being disrupted by instabilities but also damps mixing and condensation. In the first plot of Figure 4.2 the HD simulations diverge from the MHD simulations. The MHD set shows similar mas normalized to the initial cloud mass $\left(\frac{M}{M_{cl}}\right)$ until material leaving the domain becomes too great of an effect to be overcome by condensation. The time when material begins to leave the domain is marked with circles in all plots of Figure 4.2. If we instead consider only fast-cool gas ($T \leq$ 10,000 K and $v_z \geq 100$ km s^{-1}) we see the effects of deceleration on the cloud in the second plot of Figure 4.2. Simulations HDn3 and MHDn3$\parallel$ show equivalent masses until $\sim$100 Myrs. After $\sim$100 Myrs the trends diverge because HDn3 has become distended and is decelerating quickly due to a large drag force. Simulation MHDn3$\parallel$ remain more streamlined and does not suffer from as strong of a drag force. It should be noted because of MHDn3$\parallel$'s long tail material begins leaving the domain at $\sim$72 Myrs which possibly results in lower mass values. Simulations HDn4, MHDn3$\perp$, and MHDn4$\perp$ show lower values of fast-cool mass normalized to the initial cloud mass than Simulations HDn3 and MHDn3$\parallel$ but show similar values to each other. Simulation MHDn3$\perp$, with its higher initial mass, is not decelerated as quickly as Simulations HDn4 and MHDn4$\perp$. Due to Simulation MHDn3$\perp$'s long thin tail material does begin leaving the domain early in the simulation but the majority of the

fast-cool mass remains in the head of the cloud. However, due to the magnetic field damping instabilities, and therefore damping condensation, we see an overall downward trend showing that the deceleration and evaporation of mass outpaces any condensation. Simulation HDn4fragments heavily and the small light fragments decelerate and evaporate quickly. Lastly, Simulation MHDn4$\perp$ had a low mass and is quickly decelerated by both the ram and magnetic pressure. The small compressed cloud is decelerated until no fast-cool material remain in the domain by $\sim$125 Myrs.

The middle two plots of Figure 4.2 show the volume of cool ($T \leq 10,000$ K) material in the left plot and the volume of fast-cool ($T \leq$ 10,000 K and $v_z \geq 100$ km s^{-1}) material in the right plot. The volume can be interpreted as an indicator of the morphological evolution of the clouds. It can be seen in both plots that the MHD set experiences a sudden compression early in the simulations due to magnetic pressure. The MHD set once compressed begin to diverge at $\sim$25 Myrs. Simulation MHDn4$\perp$ shows an almost constant cool material volume until $\sim$125 Myrs when any fast-cool material is no longer present in the domain due to either being decelerated below the threshold speed ($v_z \geq 100$ km s^{-1}) or by being swept from the domain. Simulation MHDn3$\perp$ shows increases in cool volume but a fast-cool volume that vacillates about a value of $\sim$0.1 kpc^3. This is due to MHDn3$\perp$'s head becoming distended later in the simulation and constantly decelerating. Simulation MHDn3$\parallel$ compresses to a minimum volume at $\sim$25 Myrs and then monotonically increases in volume. The tail of Simulation MHDn3$\parallel$ is larger in volume than the thin tails of the other members of the MHD set resulting in higher volume values. The cause of the constant increase of volume is apparent in th velocity field inside the tail depicted in Figure 4.1. Ambient material is drawn toward the head of the cloud through the center of the tail. As time progresses this gas cools and fills in the low density center of the tail resulting in more volume that meets the cool and fast-cool criteria.

The HD set experiences different volume evolution. Simulation HDn4 does not show much growth because the small fragments evaporate quickly and do not account for much

volume. Simulation HDn3 however, undergoes a evolutionary event where the cool material more than doubles in volume before compressing again between ∼25 Myrs and ∼110 Myrs. This event is the cause of Simulation HDn3's strong condensation as the event entrains large amounts of ambient material. After ∼110 Myrs the cool material monotonically increases in volume while the fast-cool material decreases. This is caused by the cloud expanding in the $\hat{z}$ direction due to the tail end of the cloud decelerating and distending the cloud.

4.4 Summary and Discussion

In this study we've produced five 3-dimensional simulations of HVCs. The simulations are grouped into HD and MHD sets. From comparisons between sets we can surmise that like the smaller fountain model clouds of Kwak et al. (2009) clouds in a magnetic field parallel to the trajectory of the cloud are confined but do not decelerate as quickly as the HD counterpart or MHD counterparts when the magnetic field is perpendicular to the trajectory of the cloud. From our MHD set we can see that the cloud is protected against instabilities by the more laminar flow around the cloud head. While this protects the cloud ablation and fragmentation increasing its lifetime it also diminishes the condensation and mixing of the cloud. We find that in Simulations MHDn3$\perp$ and MHDn4$\perp$ that the orientation of the magnetic field confines the cloud to a classical head-tail structure and that in Simulation MHDn3$\parallel$ the cloud is contained but with a much thicker tail than the other members of the MHD set allowing it to condense large amounts of mass in the tail of the cloud and to expand to large volumes.

Table 4.1. Shared Simulation Parameters

Quantity	Symbol	Value
Domain x-range		-1.2 kpc $\leq x \leq$ 1.2 kpc
Domain y-range[a,b]		0.0 kpc $\leq y \leq$ 1.2 kpc
Domain x-range		-1.2 kpc $\leq z \leq$ 9.6 kpc
Spacial Resolution[c]		9 pc to 38 pc
Cloud Radius	r_{cl}	300 pc
Cloud Speed	$\lvert v_{cl} \rvert$	150 km s^{-1}
Cloud Temperature	T_{cl}	5,000 K
Ambient Temperature	T_{amb}	2×10^6 K

[a]For Simulations HDn3 & HDn4 only $\frac{1}{2}$ of the cloud is simulated. All reported masses and volumes are scaled by a factor of 2 as though a full cloud was simulated.

[b]Simulations MHDn3$\perp$, MHDn4$\perp$, & MHDn3$\parallel$ are modeled with a full cloud making the y-range -1.2 kpc $\leq y \leq$ 1.2 kpc.

[c]Simulations HDn3 & HDn4 use adaptive mesh refinement. Simulations MHDn3$\perp$, MHDn4$\perp$, & MHDn3$\parallel$ are simulated with all cells having a spacial resolution of 9 pc.

Table 4.2. Simulation Initial Parameters

Model	n_{cl} (cm^{-3})	n_{amb} (cm^{-3})	M_{cl} (r $\leq r_{cl}$) ($M_\odot$)	$\vec{B}$ (μG)
HDn3	0.4	0.001	1,354,351.1	0.0
HDn4	0.04	0.0001	135,435.1	0.0
MHDn3$\perp$	0.4	0.001	1,354,351.1	1.0 $\hat{x}$
MHDn4$\perp$	0.04	0.0001	135,435.1	1.0 $\hat{x}$
MHDn3$\parallel$	0.4	0.001	1,354,351.1	1.0 $\hat{z}$

Note. — Initial physical parameters for all simulations.

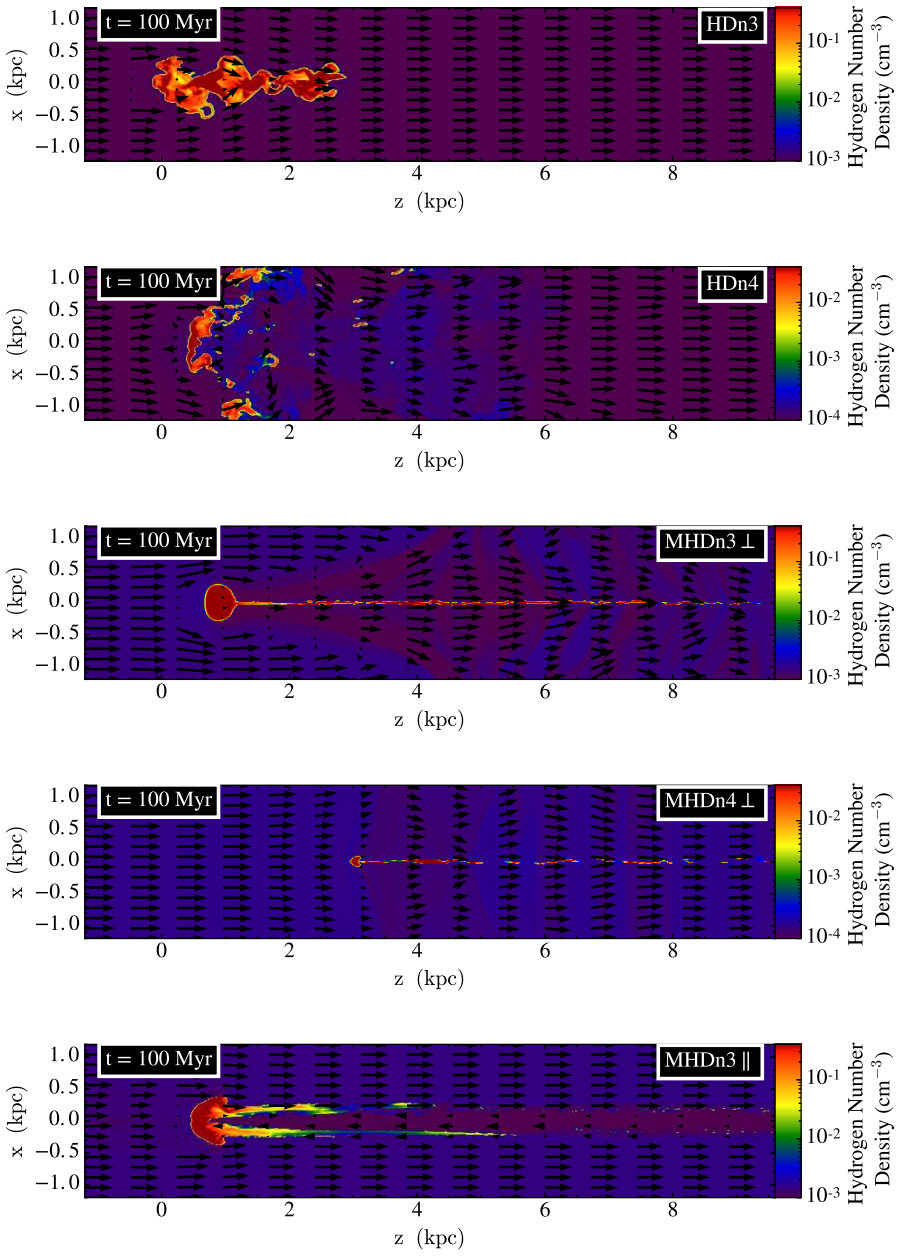

Figure 4.1: Magnetohydrodynamic Simulation Hydrogen Number Density

Each panel depicts the hydrogen number density along the $x-z$ plane for our five simulations at an arbitrary time of 100 Myrs. The velocity in the plane is annotated by black arrows for each simulation. From top to bottom we show the HD set; Simulations HDn3 and HDn4, followed by the MHD set; MHDn3$\perp$, MHDn4$\perp$, and MHDn3$\parallel$.

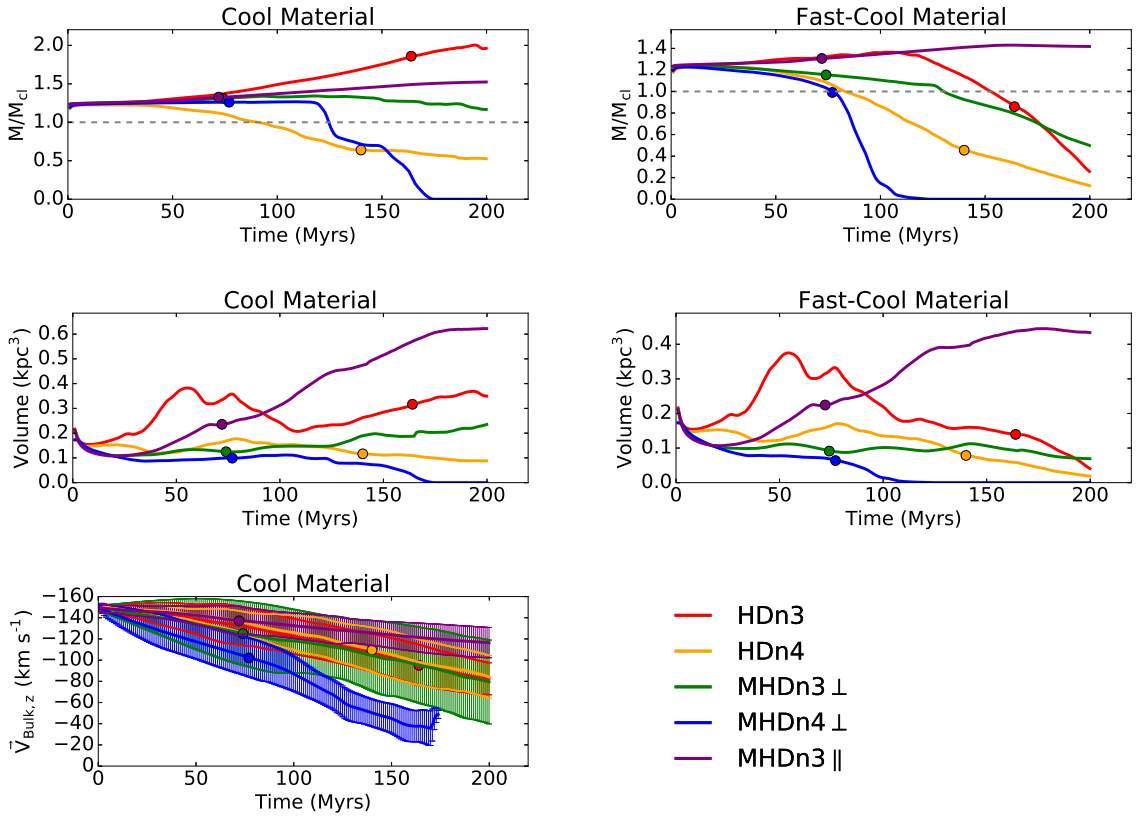

Figure 4.2: Magnetohydrodynamic High Velocity Cloud Evolution Plots

Here we plot in rows from top to bottom the mass normalized to the initial cloud mass $\left(\frac{M}{M_{cl}}\right)$, the volume of gas in the domain, and the bulk speed in the $\hat{z}$ direction which is the mass weighted average speed in the $\hat{z}$ direction. Columns of plots are differentiated by differing selection criteria for the gas. The left column only considers gas with a temperature $T \leq 10{,}000$ K while the right column only considers gas with a temperature $T \leq 10{,}000$ K and a speed in the $\hat{z}$ direction $v_z \geq 100$ km s^{-1}.

Chapter 5

Conclusions

In conclusion we have studied a variety of processes and parameters that effect the evolution of HVCs. These include mixing with the ambient environment, condensation of ambient material into the cloud, and the effects of magnetic fields on HVCs.

Using the observed metallicity of a cloud it should be possible to determine the origin of said cloud. As HVCs move through their ambient environments they interact with the ambient gas in the form of mixing. This mixing introduces ambient material into the cloud structure thereby enhancing or diluting the metal content of the cloud. We found that the concentration of ambient material by mass asymptotically approaches $\sim 30\%$ of the total mass of the cloud. By using this trend and observed metallicities of HVCs we can determine probable origins for clouds.

HVCs ablate and evaporate mass as they traverse through an ambient environment. Condensing material onto the cloud can extend the lifetime of the cloud by replacing the ablated and evaporated mass. We have shown that condensation can be a dominant process in clouds depending upon initial parameters for the clouds including; ambient density, initial cloud temperature and density, initial cloud speed, and initial cloud radius.

We have also studied the effects of uniform magnetic fields on HVCs. Clouds are effected by magnetic fields in that the magnetic field can damp instabilities on and in the cloud and confine the cloud. Both effects support the cloud against disruption increasing its lifetime, but the former effect also damps the mixing and condensation of ambient material.

Bibliography

Adams, E. A. K., Giovanelli, R., & Haynes, M. P. 2013, ApJ, 768, 77

Anders, E., & Grevesse, N. 1989, Geochim. Cosmochim. Acta, 53, 197

Bregman, J. N. 1980, ApJ, 236, 577

Burton, W. B., Braun, R., & Chengalur, J. N. 2001, A&A, 369, 616

Chandrasekhar, S. 1961, Hydrodynamic and hydromagnetic stability

Collins, J. A., Shull, J. M., & Giroux, M. L. 2007, ApJ, 657, 271

—. 2009, ApJ, 705, 962

Cooper, J. L., Bicknell, G. V., Sutherland, R. S., & Bland-Hawthorn, J. 2009, ApJ, 703, 330

Cowley, C. R., ed. 1995, An Introduction to Cosmochemistry, ISBN0521415381

Dubey, A., Fisher, R., Graziani, C., et al. 2008, in Astronomical Society of the Pacific Conference Series, Vol. 385, Numerical Modeling of Space Plasma Flows, ed. N. V. Pogorelov, E. Audit, & G. P. Zank, 145

Ferrière, K. 1998, ApJ, 503, 700

Fragile, P. C., Murray, S. D., Anninos, P., & van Breugel, W. 2004, ApJ, 604, 74

Fraternali, F., Marasco, A., Armillotta, L., & Marinacci, F. 2015, MNRAS, 447, L70

Fryxell, B., Olson, K., Ricker, P., et al. 2000, ApJS, 131, 273

Galyardt, J., & Shelton, R. L. 2016, ApJ, 816, L18

Gritton, J. A., Shelton, R. L., & Galyardt, J. E. 2017, ApJ, in press

Gritton, J. A., Shelton, R. L., & Kwak, K. 2014, ApJ, 795, 99

Heitsch, F., & Putman, M. E. 2009, ApJ, 698, 1485

Henley, D. B., & Shelton, R. L. 2015, ApJ, 808, 22

Hill, A. S., Haffner, L. M., & Reynolds, R. J. 2009, ApJ, 703, 1832

Hsu, W.-H., Putman, M. E., Heitsch, F., et al. 2011, AJ, 141, 57

Joung, M. R., Putman, M. E., Bryan, G. L., Fernández, X., & Peek, J. E. G. 2012, ApJ, 759, 137

Klein, R. I., McKee, C. F., & Colella, P. 1994, ApJ, 420, 213

Klypin, A., Kravtsov, A. V., Valenzuela, O., & Prada, F. 1999, ApJ, 522, 82

Kwak, K., Henley, D. B., & Shelton, R. L. 2011, ApJ, 739, 30

Kwak, K., & Shelton, R. L. 2010, ApJ, 719, 523

Kwak, K., Shelton, R. L., & Raley, E. A. 2009, ApJ, 699, 1775

Lehner, N., & Howk, J. C. 2011, Science, 334, 955

Lehner, N., Howk, J. C., Thom, C., et al. 2012, MNRAS, 424, 2896

Lockman, F. J., Murphy, E. M., Petty-Powell, S., & Urick, V. J. 2002, ApJS, 140, 331

Mac Low, M.-M., & Zahnle, K. 1994, ApJ, 434, L33

Malagoli, A., Bodo, G., & Rosner, R. 1996, ApJ, 456, 708

Marinacci, F., Binney, J., Fraternali, F., et al. 2010, MNRAS, 404, 1464

Marinacci, F., Fraternali, F., Nipoti, C., et al. 2011, MNRAS, 415, 1534

Melioli, C., de Gouveia dal Pino, E. M., & Raga, A. 2005, A&A, 443, 495

Mellema, G., Kurk, J. D., & Röttgering, H. J. A. 2002, A&A, 395, L13

Miura, A. 1984, J. Geophys. Res., 89, 801

Münch, G., & Zirin, H. 1961, ApJ, 133, 11

Murphy, E. M., Lockman, F. J., & Savage, B. D. 1995, ApJ, 447, 642

Pagel, B. E. J., Edmunds, M. G., Blackwell, D. E., Chun, M. S., & Smith, G. 1979, MNRAS, 189, 95

Plöckinger, S., & Hensler, G. 2012, A&A, 547, A43

Putman, M. E., Peek, J. E. G., & Joung, M. R. 2012, ARA&A, 50, 491

Raley, E. A., Shelton, R. L., & Plewa, T. 2007, ApJ, 661, 222

Santillán, A., Franco, J., Martos, M., & Kim, J. 1999, ApJ, 515, 657

Scannapieco, E., & Brüggen, M. 2015, ApJ, 805, 158

Schneider, E. E., & Robertson, B. E. 2017, ApJ, 834, 144

Sembach, K. R., Wakker, B. P., Savage, B. D., et al. 2003, ApJS, 146, 165

Shapiro, P. R., & Field, G. B. 1976, ApJ, 205, 762

Shull, J. M., Jones, J. R., Danforth, C. W., & Collins, J. A. 2009, ApJ, 699, 754

Shull, J. M., Stevans, M., Danforth, C., et al. 2011, ApJ, 739, 105

Spitzer, J. L. 1956, ApJ, 124, 20

Sutherland, R. S., & Dopita, M. A. 1993, ApJS, 88, 253

Tripp, T. M., Wakker, B. P., Jenkins, E. B., et al. 2003, AJ, 125, 3122

Turk, M. J., Smith, B. D., Oishi, J. S., et al. 2011, ApJS, 192, 9

Twarog, B. A. 1980, ApJ, 242, 242

van den Bergh, S. 1962, AJ, 67, 486

Vieser, W., & Hensler, G. 2007, A&A, 472, 141

Wakker, B. P. 2001, ApJS, 136, 463

Wakker, B. P., & van Woerden, H. 1997, ARA&A, 35, 217

Wakker, B. P., Howk, J. C., Savage, B. D., et al. 1999, Nature, 402, 388

Wolfe, S. A., Lockman, F. J., & Pisano, D. J. 2016, ApJ, 816, 81

Wolfire, M. G., McKee, C. F., Hollenbach, D., & Tielens, A. G. G. M. 1995, ApJ, 453, 673